Department of Physics and Astronomy
Heidelberg University

Bachelor Thesis in Physics
submitted by

Anouk Kaiser

born in Freiburg im Breisgau (Germany)

2023

Tracking low momentum protons with the ALICE Pixel Detector

This Bachelor Thesis has been carried out by Anouk Kaiser at the
Physikalisches Institut, Heidelberg University (Germany)
under the supervision of
Prof. Dr. Silvia Masciocchi

Abstract

This thesis focuses on alignment and tracking studies with heavy, low-momentum particles, strongly affected by multiple scattering. To this end, data from a testbeam conducted using protons of $80 - 120\,\mathrm{MeV}$ kinetic energy traversing a telescope comprised of ALICE Pixel Detector (ALPIDE) sensors is studied.
Track models ranging from the simple straight line fits to General Broken Lines trajectories, which accommodate directional changes caused by scattering, are implemented, contributing to a better understanding of the different parameters. Using these tracking models, sensor alignment is performed. The best fit parameters are determined and the track quality is assessed by means of the χ^2 formalism.
Insights into the spatial resolution of the ALPIDE sensors is provided at these energies, evaluating resolution changes under different experimental conditions. Notably, an increased inclination of the sensor planes, corresponding to increased energy loss, leads to a deterioration of the intrinsic resolution.

Zusammenfassung

Diese Arbeit konzentriert sich auf Ausrichtungs- und Spurrekonstruktionsstudien mit schweren, niedrig-energetischen Teilchen, die stark von mehrfacher Streuung beeinflusst werden. Zu diesem Zweck werden Daten aus einem Teststrahl untersucht, der mit Protonen von $80 - 120\,\mathrm{MeV}$ kinetischer Energie durchgeführt wurde, die ein Teleskop aus ALICE Pixel Detector (ALPIDE) Sensoren durchqueren.
Spurrekonstruktionsmodelle, die von einfachen Geradenanpassungen bis zu General Broken Lines Trajektorien reichen, die Richtungsänderungen aufgrund von Streuung berücksichtigen, werden implementiert und tragen zu einem besseren Verständnis der verschiedenen Parameter bei. Unter Verwendung dieser Spurrekonstruktionsmodelle wird die Ausrichtung der Sensoren durchgeführt. Die Parameter der besten Anpassung werden bestimmt und die Qualität der Spur wird mithilfe des χ^2-Formalismus bewertet.
Einblicke in die räumliche Auflösung der ALPIDE-Sensoren werden bei diesen Energien gegeben, wobei Auflösungsänderungen unter verschiedenen experimentellen Bedingungen bewertet werden. Insbesondere führt eine erhöhte Neigung der Sensorebenen, die einem erhöhten Energieverlust entspricht, zu einer Verschlechterung der intrinsischen Auflösung.

Contents

Chapter 1

A LARGE ION COLLIDER EXPERIMENT (ALICE)

ALICE is a multipurpose detector located at the Large Hadron Collider (LHC), optimised for ultra relativistic heavy-ion collisions. It is designed to study the physics of strongly interacting matter at extreme energy densities, where a phase of matter called quark-gluon plasma (QGP) forms [6].

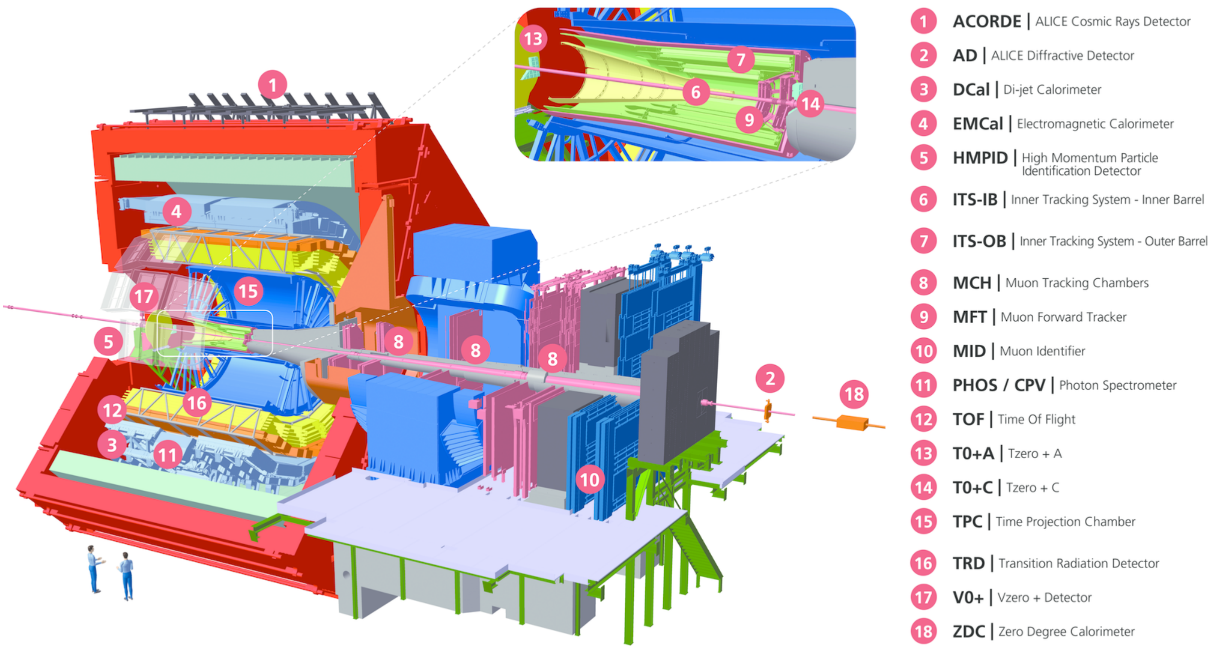

Figure 1.1: The sketch shows the composition of the ALICE detector [38].

To retrace all physical processes that happen after a high energy particle collision, several detectors are necessary. The ensemble of detectors, surrounding the interaction point, aims to study the properties of the particles that fly out. The innermost two are the Inner Tracking System (ITS) and the Time Projection Chamber (TPC). They were built

to precisely determine the vertex and then track the charged particles in the magnetic field of 0.5 T, which forces them onto a curved trajectory thus enabling momentum and charge sign measurements.
There are many other important detectors, which altogether are crucial for the successful and reliable identification and reconstruction of produced particles. The composition of the whole ALICE detector is shown in figure 1.1 and a short summary of each detector can be found in [6]. The current study focuses on tracking of low momentum particles and therefore only the main tracking devices, the ITS and the TPC, shall be discussed.

1.1 Inner Tracking System (ITS)

The main focus of the ITS is to reconstruct the primary and secondary vertices, track charged particles with a low transverse momentum (p_{T}) and improve the momentum resolution at high p_{T}. To guarantee the best possible tracking resolution for the primary vertex, the detector is placed as close as possible to the interaction point.
One of the major interests for the ALICE collaboration during the second long shutdown (LS2, 2019-2021) at the LHC was the upgrade of the ITS. The new ITS, also called ITS2, now consists of seven concentric ALPIDE[1] layers with a total active surface of about $10\,\mathrm{m}^2$.
Three design goals, instrumental for the physics programme, were considered for this upgrade. On the one hand, the readout rate was significantly increased. This was especially driven by the fact that during LS2 the LHC was enhanced to deliver Pb-Pb collisions at higher luminosity. On the other hand, the tracking resolution was improved. This was possible because the pixel detectors themselves have a better resolution compared to the previous setup, the radius of the beam pipe has been reduced, so the detectors are closer to the interaction point and the material budget has been substantially reduced, resulting in less multiple scattering and energy loss. Lastly, the tracking efficiency as well as the momentum resolution at low p_{T} was improved [37].

1.2 Time Projection Chamber (TPC)

The TPC is the main device to track charged particles and do particle identification. It is encasing the ITS. When a charged particle passes the gas filled cylinder, it produces electron-ion pairs. The charges drift to the endplates due to an electrical field and are multiplied by Gas Electron Multiplier (GEM) foils. This amplification system, coupled with new readout electronics for online data processing allows ALICE in Run 3 to record

[1]More about the ALPIDE, a CMOS pixel sensor, can be found in section 2.2.

Pb-Pb collisions at rates up to 50 kHz [6].
Additionally, the TPC is excellent at particle identification (PID). By measuring the specific energy loss $\mathrm{d}E/\mathrm{d}x$, of the crossing charged particle, its identity can be matched [44].

1.3 Tracking particles with low transverse momentum

The goal of ALICE is to study the quark-gluon plasma that forms at extremely high temperatures and densities. To access properties of the QGP a large number of measurements is required to investigate rare physics decay channels. The objective is to reconstruct these channels across a wide range of transverse momentum. However, accomplishing this task by measuring the transverse momentum with the help of a magnetic field, particularly at the extremes of the momentum range, poses significant challenges.
The latest studies especially address the requirements for enhanced and extended measurements of heavy-flavour hadrons, quarkonia, and low-mass dileptons at low transverse momenta [4, 5]. In these cases, the signal-over-background ratio is very small, which calls for an increase in statistics. This is enabled by the luminosity upgrade of the LHC combined with the online data processing of ALICE in Run 3. On the other hand, an improvement of these measurements requires an improvement in vertexing and tracking efficiency at low transverse momentum to reduce the large combinatorial background.
To address this requirement, the tracking precision was increased with the upgrade of the ITS that involved reducing the material budget and enhancing the detector resolution. These enhancements lay the foundation for improved particle reconstruction, resulting in higher efficiency for accurately reconstructing particle trajectories with precise position resolution. However, this is only half of the battle.
In order to achieve successful reconstruction, a tracking model suitable for low momentum particles is necessary. It is essential to have a model that accurately represents the path of a charged particle, closely approximating its true trajectory. Only with such a model improvements in the measurements obtained from the reconstruction process can be expected.

In this thesis, the first step is to understand the differences in trajectories between low momentum and high momentum, heavy, charged particles. Starting from the fundamental principles of charged particle detection, the process of particle track reconstruction is discussed. This forms the basis for understanding the reconstruction technique in the ALICE detector. Afterwards, other tracking models, that can be employed in experiments

with a lower particle density in the detector, are introduced. There, special emphasis is placed on the accurate representation of low momentum particles.
Using exemplary data, the performance of different tracking models in terms of their ability to handle low momentum particles is evaluated. This leads to a comprehensive discussion on the achieved tracking quality with the presented models.

Chapter 2

PARTICLE DETECTION

2.1 Passage of charged particles through matter

Measuring properties of a particle in a detector requires it to interact with the detector material. This poses a conflict between the desire to detect the particle and the desire to minimise its interaction with the sensor material. While this issue may be less problematic for particles with high momentum, it remains challenging to completely resolve for low momentum particles.

Typically, charged particles undergo various interactions, resulting in energy loss, when they pass through matter. These interactions include ionisation, excitation, transition radiation, Bremsstrahlung and Cherenkov radiation. Additionally important, especially for tracking, is the impact of multiple scattering. This leads to a significant alteration of the particle trajectory, despite the low energy transfer involved [33].

2.1.1 Energy loss by ionisation and excitation

The dominant processes for energy loss of heavy, charged particles are the ionisation and atomic excitation in the matter. In this case, "heavy" specifically refers to particles with a mass M substantially higher than the electron mass. As the projectile traverses the material, many single electromagnetic interactions occur mainly with the shell electrons of the atoms, causing the ionisation or excitation. The energy transfer involved in these interactions is a statistical process. Nevertheless, when looking at the losses for thick materials it is substantial to do the calculations with the mean energy loss.

The Bethe-Bloch formula depicts this mean energy loss $\mathrm{d}E$ per unit length $\mathrm{d}x$

$$-\left\langle \frac{\mathrm{d}E}{\mathrm{d}x} \right\rangle = Kz^2 \frac{Z}{A} \frac{1}{\beta^2} \left[\frac{1}{2} \ln \frac{2m_e c^2 \beta^2 \gamma^2 T_{\max}}{I^2} - \beta^2 - \frac{\delta(\beta\gamma)}{2} - \frac{C}{Z} \right], \tag{2.1}$$

with the following variables.

K	$4\pi N_A r_e^2 m_e c^2/A$	z	Charge of projectile
N_A	Avogadro constant	$\delta(\beta\gamma)$	Density effect correction
r_e	Electron radius	Z	Atomic number of the absorber
m_e	Electron mass	I	Mean excitation energy
A	Atomic mass of absorber	$\frac{C}{Z}$	Shell correction

Table 2.1: Variables to calculate the mean energy loss with the Bethe-Bloch formula.

T_max is the maximum kinetic energy to be transferred from the projectile particle to a free electron in a single collision and is given by

$$T_\mathrm{max} = \frac{2m_e c^2 \beta^2 \gamma^2}{1 + 2\gamma m_e/M + (m_e/M)^2}. \tag{2.2}$$

The energy loss for high, medium or low $\beta\gamma$ of the incident particle are characterised by different effects and result in the characteristic form of the Bethe-Bloch formula, which is shown in figure 2.1.

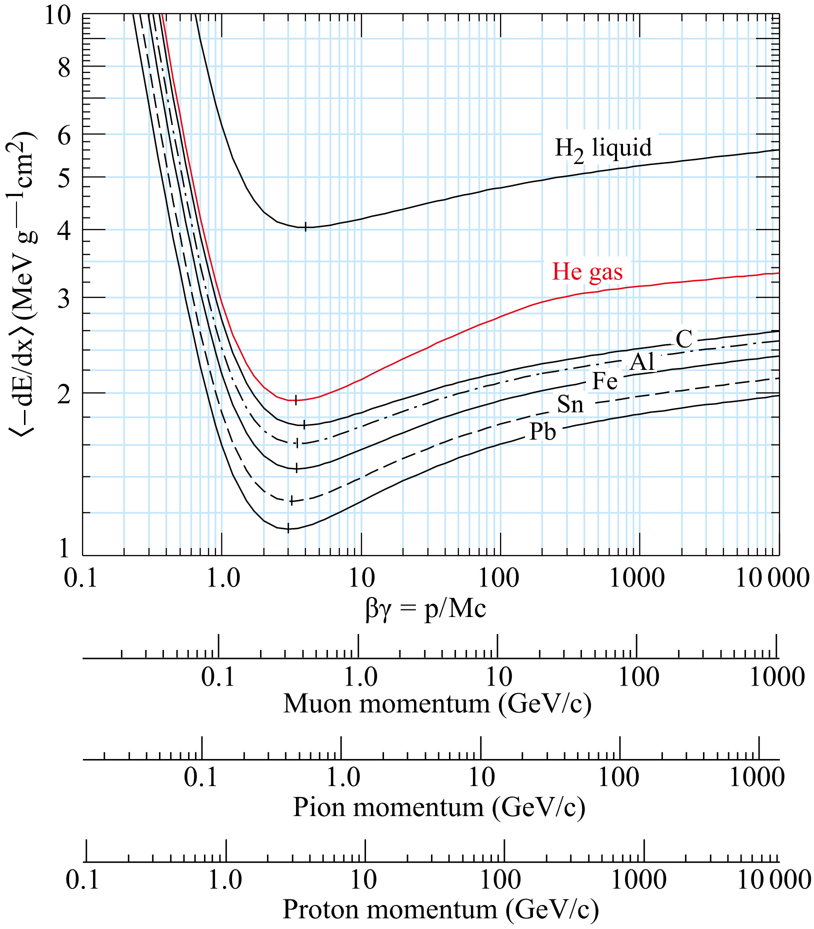

Figure 2.1: The graph shows the material density independent mean energy loss for different materials and particles [43].

The particle is minimum ionising (MIP) at $\beta\gamma \approx 3-4$. For small $\beta\gamma$ the losses quickly increase due to the increased time in the electric field of the atom. The shell correction has to be applied, since in electronic shells capture processes become possible as well as the assumption of atomic electrons to be at rest is no longer valid. For high values of $\beta\gamma$ the transverse electric field increases and therefore also the energy loss increases. However, the field extension is limited because the medium becomes polarised. This effect is included with the density correction [43].
One common variation of the Bethe-Bloch formula involves dividing it by the density of the material through which the particle is passing, resulting in a quantity known as the mass stopping power [26]. This is because the energy loss of a charged particle is proportional to the number of atoms or electrons in the material that it interacts with, and the density of the material is a measure of the number of these interaction sites per unit volume. This normalised form of the formula allows to compare the stopping power of different materials and particles, regardless of their density or thickness.

2.1.2 Multiple Coulomb scattering

A charged particle heavier than an electron elastically scatters in material. The deflection predominately occurs in the Coulomb field of the atomic nucleus. The probability density function for the scattering angle θ of a single interaction is derived from the Rutherford scattering formula. In a prolonged material many small scatterers result in a net angle distribution that approximates a Gaussian shape. This is due to the central limit theorem. However, in thin scatterers, less frequent "hard" scattering events contribute to non-Gaussian tails.
The angle distribution can be approximated by a normal mixture with two components (a double Gaussian) [19]. One component models the core and the other models the tails of the distribution. Following the Molière theory, the associated core Gaussian distribution has a mean $\mu = 0$ and standard deviation

$$\theta_0 = \frac{13.6\,\mathrm{MeV}}{\beta c p} z \sqrt{\frac{x}{X_0}} \left[1 + 0.038 \ln\left(\frac{x z^2}{X_0 \beta^2}\right)\right]. \tag{2.3}$$

Here, p, βc, and z represent the momentum, velocity, and charge number of the projectile particle, respectively, while x/X_0 denotes the material thickness in units of radiation lengths. In practical terms, the angle distribution is typically approximated as following a single Gaussian distribution with the aforementioned parameters.
The scattering angle is commonly analysed separately in two dimensions. For example, when a particle propagates parallel to the z axis, the scattering angles are denoted as θ_x and θ_y. These projected angles are uncorrelated.

Another essential quantity for describing the impact of multiple scattering is the offset y, which indicates the positional change of the passing particle. Figure 2.2 displays the offset along with other associated quantities [43]. In scenarios involving thin scatterers, the offset is typically negligible in comparison to the spatial resolution of the surrounding detectors.

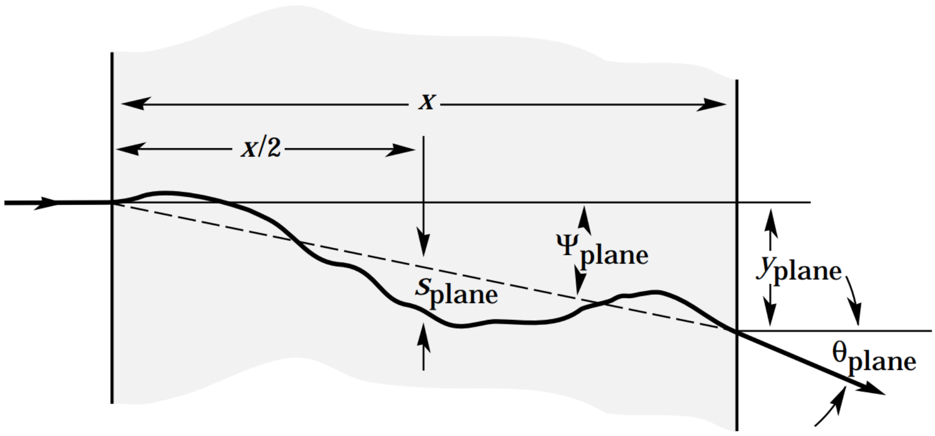

Figure 2.2: The sketch shows the quantities needed to describe multiple scattering in matter. The projectile enters the matter coming from the left, undergoes multiple interactions with the nuclei and exits the material with an offset and an angle with respect to its initial trajectory [43].

2.2 ALICE Pixel Detector (ALPIDE)

Modern particle detectors typically consist of multiple layers of sub-detectors, each designed to observe specific properties of particles. These detectors can be categorised into tracking detectors, calorimeters, and triggers. In this discussion, the main focus is on tracking devices, which reveal the paths of charged particles. Tracking detectors rely on the ionising property of charged particles and play a crucial role for the quality of the physics results of experiments.

In collider experiments, the first tracking layer is typically positioned as close as possible to the primary collision point. This strategic placement for enhancing the vertex resolution imposes specific requirements on the detector. Firstly, it must withstand extremely high particles fluxes and hence must be resistant against radiation damage. Secondly, the readout system must be exceptionally fast. Additionally, the first detector layer should possess excellent spatial resolution to enhance the vertex resolution.

These demands have motivated the utilisation of high-granularity solid-state detectors. The progress in silicon detector technologies has been remarkable over the past four decades, largely due to the rapid advancements in semiconductor technologies. The increased demand for silicon devices, driven by a growing market, has made them more affordable for particle physics research.

The ALICE Pixel Detector is a CMOS silicon pixel detector based on Monolithic Active Pixel Sensor (MAPS) technology [37]. It was developed for the recently installed upgrade of the Inner Tracking System of the ALICE experiment. The chip measures 15 mm×30 mm and is segmented into 512 × 1024 digital pixels each measuring 26.88 µm × 29.24 µm.

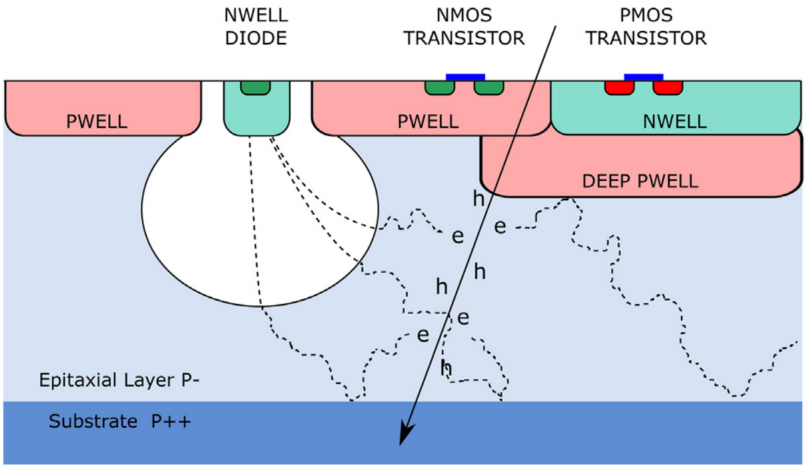

Figure 2.3: A schematic cross-section of an ALPIDE sensor. When a charged particle passes through a pixel, it liberates charge carriers through ionisation. Free electrons have the ability to diffuse within the epitaxial layer. These electrons will diffuse and subsequently drift in the vicinity of the collection diode. Eventually, they will generate a signal at the input of the pixel front-end [2].

The schematic cross-section of an ALPIDE is depicted in figure 2.3. The ALPIDE chip is implemented in a 180 nm CMOS Imaging Process provided by Tower Semiconductor Ltd. [41]. The circuits are built on a high resistivity epitaxial layer which is fabricated on a p-type substrate. A charged particle produces electron-hole pairs by ionisation. The electrons diffuse in the epitaxial layer while being confined by the potential barriers of the p-wells and the p-type substrate. Small n-well diodes in the middle of the pixel sense currents induced by electrons in the depletion volume.

A reverse bias voltage can be applied to the substrate. This bias increases the depletion volume, which leads to smaller capacitance and faster, more local charge collection, which increases the signal to noise ratio. The chip achieves a detection efficiency for MIPs better than 99 % while the fake hit rate is kept less than 10^{-6}/ pixel/ event [30]. In summary, the ALPIDE successfully meets the project requirements set by the ALICE collaboration for the upgrade of the ITS. It possesses high radiation tolerance, enables fast readout, and delivers exceptional spatial resolution.

2.2.1 Clustering

A hit on an ALPIDE pixel generates a binary yes/no information. When the amount of charge that is collected in a pixel reaches a threshold the analogue signal is converted to a digital one. Therewith, all information about the initial energy loss of the particle in the pixel is lost. Typically, a particle that traverses the detector produces more than one pixel hit on the plane. This is caused by charge sharing. Charge carriers that are freed diffuse randomly within the epitaxial layer. This makes it possible to reach several read out diodes, since the pixels are not isolated at their borders. The cluster size is dependent on the energy loss of the particle as well as the threshold settings.

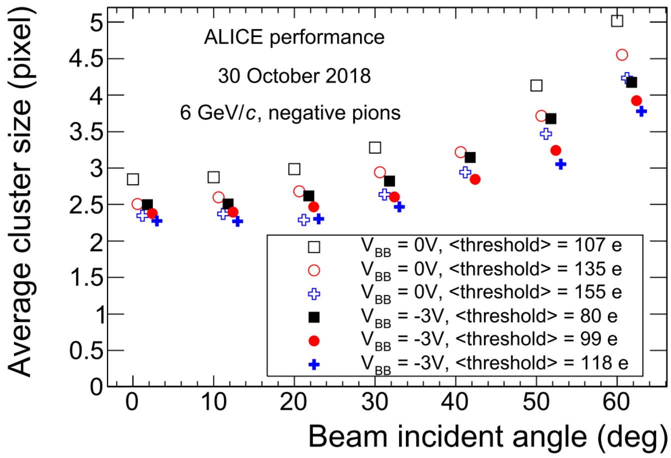

Figure 2.4: The plot depicts the average cluster size that was produces by 6 GeV/c pions in the ALPIDE chip. It shows that the cluster size increases with a higher incident angle of the particles as well as with a lower threshold value. Taken from [29].

A rotation in the detector planes results in an increase in cluster size. On the one hand this can be explained because the particle geometrically can pass several pixels at once and on the other hand the material on its way is increased resulting in more charge carriers that are freed. Figure 2.4 depicts the change in cluster size for different incident angles and different thresholds.

2.2.2 Spatial resolution

The ALPIDE chip reaches a sub-pixel pitch spatial resolution (i.e. better than pitch/$\sqrt{12}$) because of its nature concerning charge sharing. If a cluster is formed the hit position is calculated as the centre of gravity of the individual pixels that have fired. Depending on where the particle has passed, different cluster sizes are more or less probable. When particles hit the sensor at the centre, the average cluster size is below two. On the other hand, if they hit closer to the corner of a pixel the probability for higher cluster size increases.

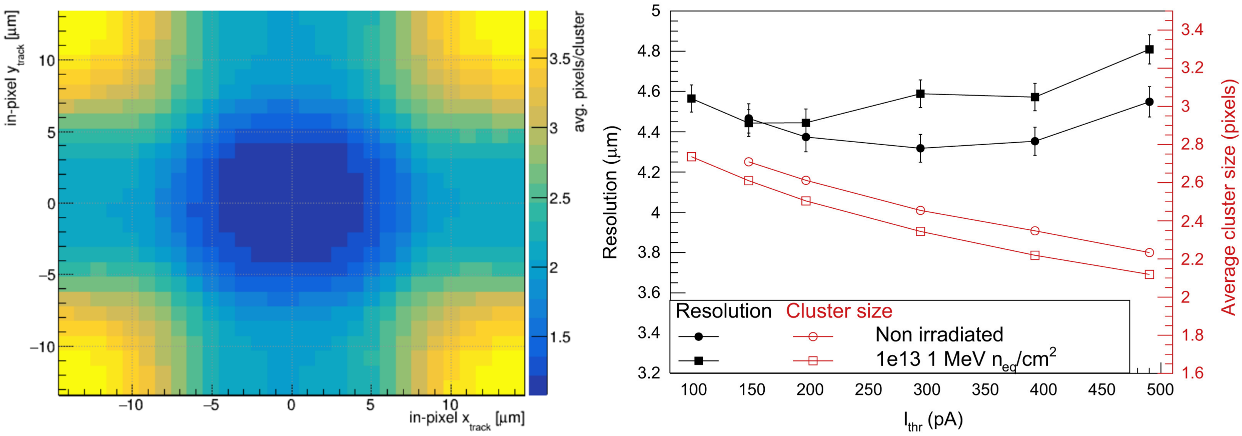

(a) (b)

Figure 2.5: (a) shows the in-pixel average cluster size dependency of an ALPIDE for minimum ionising particles that hit the detector perpendicular [27]. (b) shows the dependency of the spatial resolution on the cluster size and the threshold current [30]. The best resolution is achieved with a mean cluster size of $2.5 - 3$.

Figure 2.5a shows a pixel and highlights the region where a particular cluster size is most likely to have been generated. The ALPIDE exhibits a spatial resolution of 5 µm in both x and y dimensions, as demonstrated through studies involving minimum ionising particles that traverse the detector perpendicular to its surface. Achieving this resolution, or even better, can be accomplished by adjusting the threshold such that the average cluster size is $2.5 - 3$. The relation between spatial resolution and threshold is depicted in figure 2.5b. When particles interact with the sensor at an inclined angle, the resolution is affected due to changes in the cluster size. Smaller clusters become less frequent and the mean cluster size rises resulting in a worse spatial resolution.

Chapter 3

PARTICLE TRACK RECONSTRUCTION

This chapter will cover the scope of particle track reconstruction. First, The basic concept of hits on the detector planes will be discussed. Variables will be developed by assigning a trajectory to groups of hit points in order to trace the initial particle. Then, the introduction of the χ^2-distribution will provide the necessary mathematical background for examining the variables during the fitting process.
Additionally, specific methods will be presented for particle reconstruction, ranging from large-scale to small-scale experiments. The track model utilised in ALICE, where a high multiplicity of particle hits is encountered, will be introduced and managed using a local fit model. Furthermore, global track models will be discussed, which are specifically applicable to the analysis conducted in this study and are commonly employed for low multiplicity particle tracking.
In the scope of this thesis vectors are written as $\mathbf{v}$, matrices as $\mathbf{M}$ and scalars as v.

A tracking detector i at position z_i records the location of ionising particles passing through it and reports the hit or cluster position $\mathbf{m}_\mathrm{i}$ with the corresponding detector resolution σ_i. The z-coordinate indicates the approximate direction of flight of the incoming particles. Accordingly, a collection of hits in multiple tracking layers positioned on the z-axis, as shown in figure 3.1, can be linked to a single particle. This is a crucial stage in the track reconstruction process, as it is not always evident which hit corresponds to which particle. At the next step, a fit model is chosen and applied based on the physical processes the particle is affected by while passing the detectors. In high hit density regions, the hit assignment and track building process are applied simultaneously by iterating through the layers. This is called a **local** approach, whereas the hits are already assigned before the fitting procedure for a **global** method.

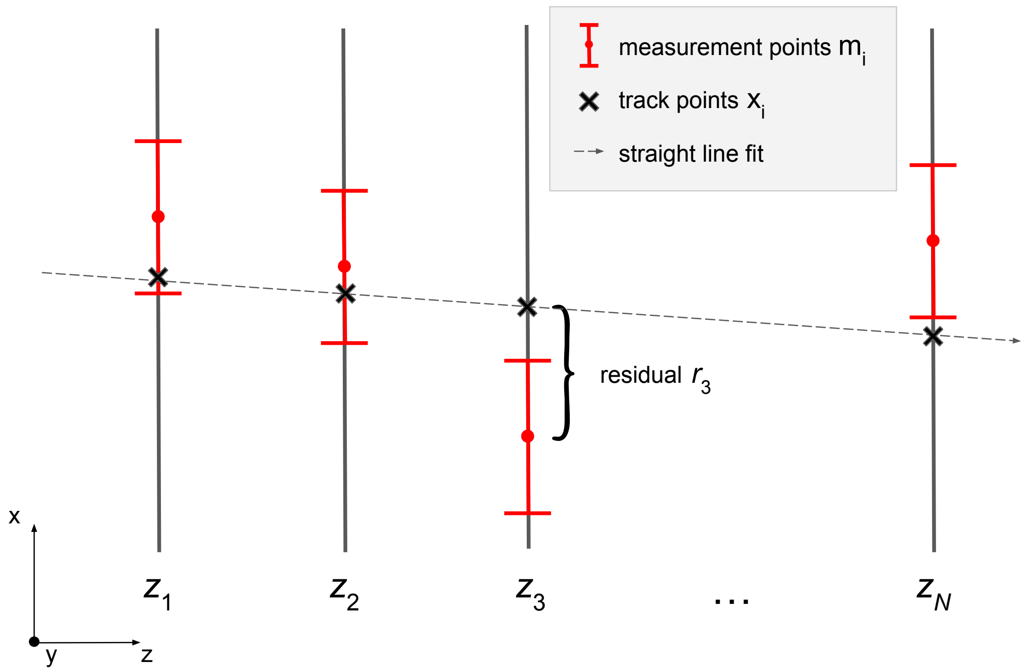

Figure 3.1: A schematic of a particle traversing N tracking detector layers, where a straight line fit is employed based on the measurement points. The fitting process generates residuals r_i that can provide valuable insights into the quality of the fit.

The distance between the measurement point $\mathbf{m}_\mathrm{i}$ and the crossing location of a track $\mathbf{x}_\mathrm{i}$ at a given layer i is called the residual

$$\mathbf{r}_\mathrm{i} = \mathbf{m}_\mathrm{i} - \mathbf{x}_\mathrm{i}. \tag{3.1}$$

The residuals are the basis for the popular reduced chi-squared statistic. This method is used to do parameter estimation for track models and to evaluate the fit quality.

3.1 Chi-square distribution

To determine the goodness of a fit the χ^2 is calculated as the squared residual ${r_\mathrm{i}}^2$ in each dimension from equation 3.1 normalised to the squared uncertainties ${\sigma_\mathrm{i}}^2$ of the measurement and summed over all N measurement points

$$\chi^2 = \sum_{\mathrm{i}=1}^{N} \frac{(m_\mathrm{i} - x_\mathrm{i})^2}{{\sigma_\mathrm{i}}^2}. \tag{3.2}$$

If the measurements are uncorrelated and normal distributed variables, the χ^2 follows the subsequent probability density function (pdf). A derivation can be found in [11].

$$f(\nu, x) = \frac{1}{2^{\nu/2}\Gamma(\nu/2, x)} x^{\nu/2-1} e^{-x/2}, \tag{3.3}$$

where ν is the number of degrees of freedom of the imposed fit and $\Gamma(\nu, x) = \int_0^\infty x^{\nu-1} e^{-x} dx$ is the Gamma function. The number of degrees of freedom, often abbreviated as ndof, is determined by the number of measurement points N minus the number of parameters M needed to describe the fit model.

Having correlated measurements on different planes i and j requires a little more consideration. The χ^2 is calculated as follows:

$$\chi^2_{\mathrm{W}} = \sum_{\mathrm{i}=1}^{N} \sum_{\mathrm{j}=1}^{N} [m_{\mathrm{i}} - x_{\mathrm{i}}] \, C^{-1}_{\mathrm{ij}} \, [m_{\mathrm{j}} - x_{\mathrm{j}}] \, . \tag{3.4}$$

C represents the covariance matrix, which provides information about the uncertainties and correlations of the terms $[m_{\mathrm{i}} - x_{\mathrm{i}}]$ and $[m_{\mathrm{j}} - x_{\mathrm{j}}]$.

Tracking detectors often produce correlated measurements due to various factors. For instance, in the case of strongly scattered particles, the scatterers in each detector can influence the position measurements of the particles further downstream, leading to correlation between the measurements. As a result, the sum includes mixed residual terms from different planes, with their appropriate contribution given by the inverse of the covariance matrix.

Deriving the probability density function of χ^2_{W} requires a mathematical approach. The covariance matrix needs to be diagonalised so the sum can be written with uncorrelated terms. The new random variables are formed by linear combinations of the original variables. By scaling the variables so they absorb the eigenvalues of the diagonal covariance matrix, the matrix is left with $N - M$ 1's on the diagonal and M 0's. In practice, the resulting equation has a pdf that is distributed as $f(\nu, x)$ again [7].

The pdf of a chi-square sum has a mean that is equal to the number of degrees of freedom ν and a mode (peak) that is given by $\max(\nu - 2, 0)$. The probability density functions for different ndof's are shown in figure 3.2.

For high numbers of degrees of freedom the mode divided by the mean converges to one, which explains the commonly know quality check, where the reduced chi-square[1] peak is expected to be one. An alternative way to confirm the fit quality is to check if the mean of the reduced χ^2 is one or respectively the mean of the χ^2 itself is equal to the degree of freedom.

[1] To calculate the reduced chi-squared χ^2_{red}, the χ^2-value is divided by ν.

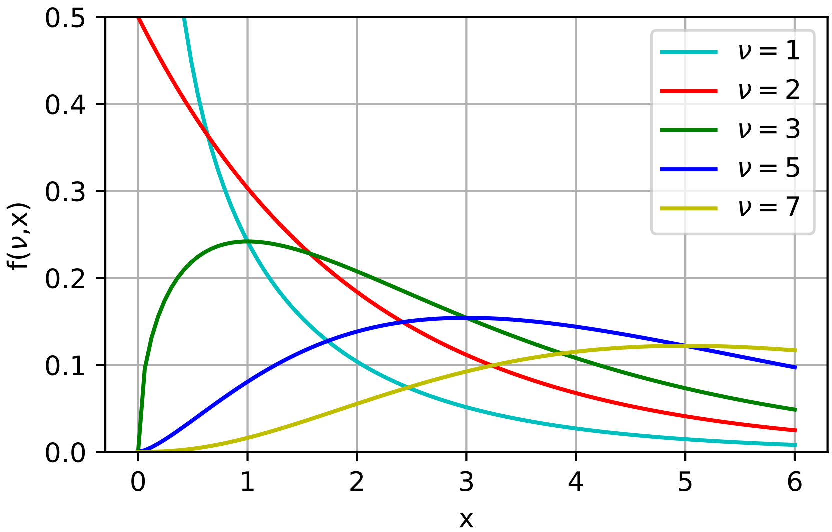

Figure 3.2: This plot shows the probability density function of a χ^2-sum for different numbers of degrees of freedom ν following equation 3.3.

Although this quality check is consistently applicable, it is not easily detectable by the naked eye.

The fit quality is good when the calculated χ^2-distribution follows the associated probability density function. If this is not the case, it is important to know how to interpret these ambiguities. In general, a chi-square distribution, that peaks at lower values than it is supposed to, indicates that the uncertainties of the measurements are overestimated. On the other hand, a distribution peaking at higher values can indicate an underestimation of the uncertainties.

In the context of tracking, this is not the only possible explanation. A difference to the theoretical expectation can also be caused by a wrong fit model or a misalignment in the setup. These negative effects on the χ^2-distribution will be illustrated in section 4.1.3 using an example.

3.1.1 Minimisation of chi-square for parameter estimation

The chi-square is not only used to determine the fit quality, but also to calculate the best fit variables. By varying the parameters and minimising the chi-square value, the best fit can be obtained. Mathematically, it can be expressed as follows:

The track point x_i is calculated using a polynomial of degree L. This polynomial is a linear function of the parameter array $\mathbf{a} = (a_1, a_2, ..., a_{L+1})^\mathrm{T}$ evaluated at the position of the measurement z_i

$$x_\mathrm{i} = g(z_\mathrm{i}; \mathbf{a}) = a_1 \cdot {z_\mathrm{i}}^0 + a_2 \cdot {z_\mathrm{i}}^1 + a_3 \cdot {z_\mathrm{i}}^2 + ... + a_{L+1} \cdot {z_\mathrm{i}}^L. \tag{3.5}$$

χ^2 therefore is

$$\chi^2 = \sum_{\mathrm{i}=1}^{N} \frac{(m_\mathrm{i} - g(z_\mathrm{i}; \mathbf{a}))^2}{\sigma_\mathrm{i}{}^2} \tag{3.6}$$

and can be derived with respect to each parameter a_l in $\mathbf{a}$:

$$\frac{\partial \chi^2}{\partial a_\mathrm{l}} = 0. \tag{3.7}$$

To find the minimum, the derivative is set to zero. The resulting equation can then be solved to obtain the best fit parameters.

3.2 Tracking in ALICE: a local track model

Different tracking detector setups, characterised by varying conditions such as particle density, material budget, or magnetic fields, necessitate the availability of a diverse range of track models that are tailored to meet specific requirements. In the subsequent sections, various track models will be introduces. By examining the advantages and disadvantages associated with each approach, the situations in which they can effectively reconstruct particle trajectories can be determined.

The first example for a track model can be given by the local method employed in ALICE. Finding the accurate pattern of each individual particle through global fits among all recorded hit combinations based on the smallest χ^2-value given by the fit is not a feasible approach. This is primarily because of the enormous number of possible hit combinations assigned to one particle given the high luminosities provided by the LHC.

Therefore, tracking in ALICE is done by an algorithm based on a local track model: Kalman filtering. It provides a simultaneous recognition and reconstruction of particle tracks in the TPC and the ITS with a relatively low computing time (increasing linearly with the number of planes involved). In simple terms, this is achieved by reconstructing a track step by step, or rather layer by layer. At each plane, a predicted region of interest is determined based on the physics processes that can occur (e.g. multiple scattering) and indicates where the next tracking point is most likely to be found. This means that not every combination of the measured points needs to be determined [42]. A simplified example is depicted in figure 3.3.

The algorithm has to be seeded a-prior with an initial guess for the trajectory. This is usually done in regions of lower occupancy. There, spatially adjacent measurement points are combined to build small track seeds. The lower the multiplicity in this region is, the more successful it is to correctly match the hit points created by the particle being tracked. Seeding is essential for a good reconstruction since the initial trajectory is followed to find further belonging hits in denser regions closer to the collision point.

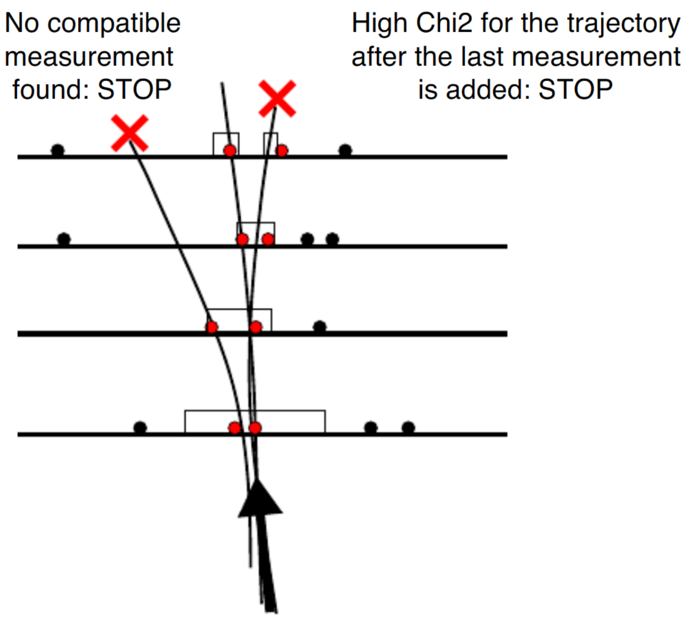

Figure 3.3: Schematic representation of the Kalman filter based pattern recognition. The red and black points represent hits that were detected on four layers of a detector during a specific time frame. The black arrow depicts the seed for the algorithm. The rectangles indicate the areas (search windows) where a hit is expected based on extrapolation from the Kalman filter. Only the red points fall within these windows, resulting in three possible particle trajectories. Two of them are rejected, one due to the lack of compatible measurements in the outer layers and the other due to a high χ^2-value. The remaining trajectory most likely represents a true particle [1].

3.2.1 Kalman filter

The Kalman filtering technique originates from the requirement to estimate the trajectory of a dynamical system in real time. Hence, at the time a prediction shall be made, only information about the past intersection points of a particle with the detectors are available. With this knowledge a prediction for the whole trajectory can be made. This prediction gets updated as new measurements are included and subsequently gets better and better. The algorithm has numerous technological applications like the guidance, navigation, and control of vehicles, robotic motion planning and of course trajectory optimisation, to name just a few [3].

The process is split into three main operations: **prediction**, **update** and **smoothing**. To mathematically go through these steps a few basic quantities and equations are needed that closely follow the discussion in [16, 32, 9].

The fundamental component is a state vector $\mathbf{s}_\mathrm{i}$, which describes the track properties at a plane i, and its covariance matrix $\mathbf{C_i}$. The assumption of a discrete linear Kalman filter is, that the evolution of the state vector to the vector describing the track at the next plane, is a linear transformation $\mathbf{T}_\mathrm{i}$ plus a random normal disturbance $\mathbf{w}_\mathrm{i}$ with $\langle \mathbf{w}_\mathrm{i} \rangle = 0$

and its covariance matrix $\mathbf{W}_\mathrm{i}$:

$$\mathbf{s}_\mathrm{i} = \mathbf{T}_{\mathrm{i}-1}\mathbf{s}_{\mathrm{i}-1} + \mathbf{w}_{\mathrm{i}-1}. \tag{3.8}$$

The transformation underlies the physical processes and forces that the particle is affected by while traversing the detector planes. In this context of ALICE (a charged particle in a homogeneous magnetic field), a helix is the model to choose, while the disturbance represents the effect of multiple scattering. Although a helix is a non-linear equation it can be locally approximated by a linear function by taking the first two terms of its Taylor series expansion.

The measurement on the current plane is described by the vector $\mathbf{m}_\mathrm{i}$ and its covariance matrix $\mathbf{V}_\mathrm{i}$. A coordinate system fitting the measurement space is chosen. Therefore, the covariance matrix is diagonal. To compare the track position $\mathbf{x}_\mathrm{i}$ on the plane with the measurement a matrix $\mathbf{H}_\mathrm{i}$ is needed to describe the transformation from the state vector into the measurement space:

$$\mathbf{x}_\mathrm{i} = \mathbf{H}_\mathrm{i}\mathbf{s}_\mathrm{i}. \tag{3.9}$$

Finally, the processes of the Kalman filter can be described. Starting with a prior knowledge of the state or a former state vector respectively, the first step is the **prediction** of the state vector for the current plane. A transformation matrix multiplied with the former states vector states the most probable current state vector. The true particle trajectory also has a disturbance from multiple scattering. However, this is not included in the prediction for the state vector since the most probable value for the disturbance is zero.

$$\mathbf{s}_\mathrm{i}^{\mathrm{i}-1} = \mathbf{T}_{\mathrm{i}-1}\mathbf{s}_{\mathrm{i}-1} \qquad \mathbf{C}_\mathrm{i}^{\mathrm{i}-1} = \mathbf{T}_{\mathrm{i}-1}\mathbf{C}_{\mathrm{i}-1}\mathbf{T}_{\mathrm{i}-1}^\mathrm{T} + \mathbf{W}_{\mathrm{i}-1}. \tag{3.10}$$

Hereby, the superscript digit denotes the impact of the state vector $\mathrm{i}-1$. If the superscript is smaller than the current number as in equation 3.10, the variable is a prediction and not yet a fitted track point itself. The estimated residual $\mathbf{r}_\mathrm{i}$ and its covariance $\mathbf{R}_\mathrm{i}$ become

$$\mathbf{r}_\mathrm{i}^{\mathrm{i}-1} = \mathbf{m}_\mathrm{i} - \mathbf{H}_\mathrm{i}\mathbf{s}_\mathrm{i}^{\mathrm{i}-1} \qquad \mathbf{R}_\mathrm{i}^{\mathrm{i}-1} = \mathbf{V}_\mathrm{i} + \mathbf{H}_\mathrm{i}\mathbf{C}_\mathrm{i}^{\mathrm{i}-1}\mathbf{H}_\mathrm{i}^\mathrm{T}. \tag{3.11}$$

The prediction is the main feature of a Kalman filter for ALICE, because it offers the step wise build-up of the trajectory. The estimated state vector is calculated and states where the next measurement point can be found. By allowing only a certain deviation of the estimated track point and the measurement, a filter for all existing hits on the plane is achieved.

The next step, **update**, is done after every prediction. The state vector will be updated based upon the current and all past measurements. Hence, the fit parameters for the helix are updated to achieve the minimal χ^2, resulting in a new estimate of the state vector

$$\mathbf{s}_\mathrm{i} = \mathbf{s}_\mathrm{i}^{\mathrm{i}-1} + \mathbf{K}_\mathrm{i}(\mathbf{m}_\mathrm{i} - \mathbf{H}_\mathrm{i}\mathbf{s}_\mathrm{i}^{\mathrm{i}-1}) \qquad \mathbf{C}_\mathrm{i} = (\mathbb{1} - \mathbf{K}_\mathrm{i}\mathbf{H}_\mathrm{i})\mathbf{C}_\mathrm{i}^{\mathrm{i}-1} \tag{3.12}$$

$$\mathbf{K}_\mathrm{i} = \mathbf{C}_\mathrm{i}^{\mathrm{i}-1}\mathbf{H}_\mathrm{i}^\mathrm{T}(\mathbf{V}_\mathrm{i} + \mathbf{H}_\mathrm{i}\mathbf{C}_\mathrm{i}^{\mathrm{i}-1}\mathbf{H}_\mathrm{i}^\mathrm{T})^{-1}. \tag{3.13}$$

with the Kalman gain matrix $\mathbf{K}_\mathrm{i}$. The gain matrix incorporates the corrections derived from minimising the χ^2. The minimisation process requires matrix inversions. The local model offers the advantage of inverting only small matrices, which leads to a faster computation.

The state vector at the last filtered point n contains the full information to calculate the state vector of any point i already tracked. Hence, the full trajectory can be determined. It is a recursive operation in the direction opposite to the filter process and described by the **smoothing** equations:

$$\mathbf{s}_\mathrm{i}^\mathrm{n} = \mathbf{s}_\mathrm{i} + \mathbf{A}_\mathrm{i}(\mathbf{s}_{\mathrm{i}+1}^\mathrm{n} - \mathbf{s}_{\mathrm{i}+1}^\mathrm{i}) \qquad \mathbf{C}_\mathrm{i}^\mathrm{n} = \mathbf{C}_\mathrm{i} + \mathbf{A}_\mathrm{i}(\mathbf{C}_{\mathrm{i}+1}^\mathrm{n} - \mathbf{C}_{\mathrm{i}+1}^\mathrm{i})\mathbf{A}_\mathrm{i}^\mathrm{T}. \tag{3.14}$$

$$\mathbf{A}_\mathrm{i} = \mathbf{C}_\mathrm{i}\mathbf{T}_{\mathrm{i}+1}^\mathrm{T}(\mathbf{C}_{\mathrm{i}+1}^\mathrm{i})^{-1}. \tag{3.15}$$

with $\mathbf{A}_\mathrm{i}$ the smoother gain matrix. The matrix holds the information on how to move upstream with the correct fit parameter for the model as well as the process noise from multiple scattering associated with the current plane. The smoothed trajectory therefore contains kinks. Here, the superscript digit is bigger than the plane under observation. This indicates that the state vector already incorporates the updates from the measurements up to the plane indicated by the superscript.

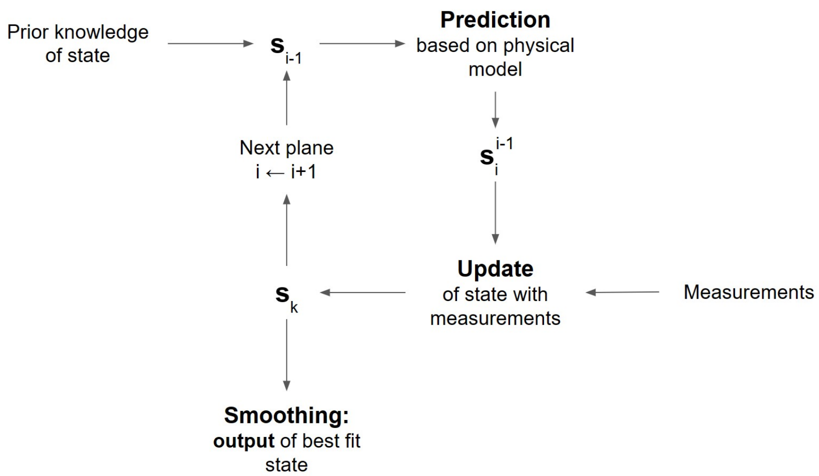

Figure 3.4: The diagram, adapted from [3], shows the basic process loop of a Kalman filter. The process begins with a prior knowledge state vector serving as the initial prediction for the current plane. Then, the current state vector is updated with measurement information and a new prediction is made by incrementing through the planes.

In summary, the three steps **prediction**, **update** and **smoothing**, that build a cycle, are depicted in figure 3.4. A prior knowledge of the first state vector is very beneficial to be able to make the first prediction as truthful as possible. The prediction is based on the underlying physical process and after every filter step the updated state vector of any tracked plane can be computed. The loop increments by moving one plane further. The Kalman method has many advantages. Nevertheless, there are also a few shortcomings. The most crucial one is, that a realistic initial approximation for the state vector is needed to enable a stable and successful filtering procedure [9].

3.2.2 Seeding

There are different option to do seeding depending on the circumstances. In general, a distinction is made between internal and external seeds. If the particle trajectory is coarsely known before starting the reconstruction procedure the seed is external. This is applicable, for instance, when another detector within the experiment provides information about the track, or when the particle is deliberately directed into the tracking detector. An internal seed is required when there is a lack of external information available regarding the particle to be tracked and has the form of a track itself but with fewer measurement points, hence it is called tracklet.

Even though other detectors in ALICE provide some information about the particle tracks, this external seed is too vague combined with the high multiplicities, to successfully start a reconstruction on its own.

The tracking algorithm in ALICE relies on an internal seed that is constructed at the outer most hit point in the TPC, since the hit density is significantly lower there, hence, it is easier to find the correct seed for the true trajectory of a charged particle. Is not trivial to have a successful yet fast procedure to find a good internal seed, representing the initial state vector.

The developed seeding algorithm for Run 3 is based on the cellular automaton principle [36] and is a two-stage combinatorial process depicted in figure 3.5.

First, spatially adjacent clusters are connected, building tracklets. This eliminates non-physical combinations, as physics only allows charged particles to deviate by a certain degree from their initial path. Therefore, clusters that are not found within a certain spatial proximity cannot be produced by the same particle.

Secondly, for each cluster, the best pair of neighbouring clusters on the previous and following row is determined on the basis of the best straight line that these three cluster form and on loose vertex constraints. The criteria of the straight line is sensible, because at correspondingly small scales the helix path of the particle is almost straight. Furthermore, including the vertex constrain assures that the particles actually originate from the collision, but since they possibly do not come from the primary vertex, these cuts must not be very strict.

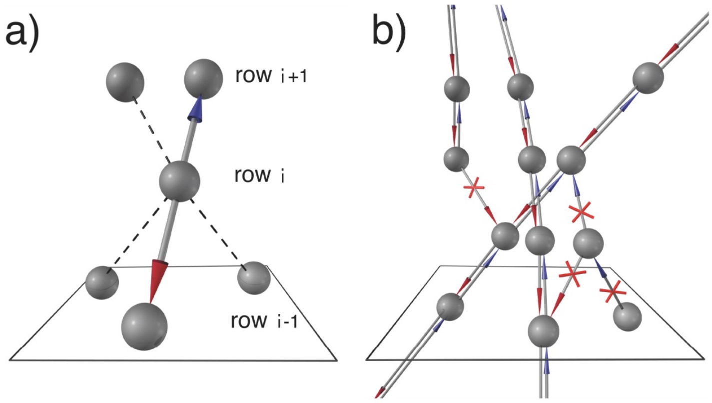

Figure 3.5: This figure show the basic principal of the two step cellular automaton seeding algorithm [36]. a) Finding the best pairs of neighbours and connecting them to tracklets. b) Non-reciprocal links are removed, following certain criteria.

3.3 Global track models

When small scale experiments are conducted, the problem of track finding and track multiplicity can typically be avoided. This is achieved by operating with low particle rates, which allows the measurement points of different particles to be separated in time. Using a trigger, only one particle track is recorded at a time, allowing for efficient analysis using global fits. As a result, global fits are often the preferred and quickest solution in such cases.

Particles, heavier then electrons and above certain momenta will follow an almost straight line, as long as they are not affected by outer forces like a magnetic or electric field. If detectors were able to track the particles without them having to interact, the particle path would remain unchanged. To reconstruct the trajectory, the least square method is often used to fit a straight line and obtain high-quality tracks. This assumption of particles following a straight line unaffected by the detector can be applied when studying relativistic particles, as their energy loss in matter is negligible compared to their momentum, and the impact of multiple scattering is small. However, when examining low-momentum particles, the trajectory changes at every detector plane and in the air between the planes because of multiple scattering. Therefore, ignoring these effects can lead to a poor fit quality. It is essential to account for these factors by employing appropriate fit models to achieve accurate results.

In the following discussion, three global track models are introduced. For relativistic particles or those minimally affected by multiple scattering, an unweighted straight line model is primarily utilised. This model incorporates each measurement with its respective measurement resolution without applying additional weights. On the other hand, for low-momentum particles that experience strong scattering in traversed matter, a weighted straight line fit is more suitable. This model assigns different weights to individual measurements during the fitting process, considering the varying degrees of scattering effects encountered by the particles. Lastly, the concept of a broken line trajectory method is introduced, which aims to replicate the behaviour of particles that undergo substantial direction changes as they traverse the detector material. The broken line approach involves fitting the particle's trajectory using multiple straight line segments, allowing for abrupt changes in direction.

3.3.1 Unweighted straight line

For massive relativistic particles passing through a tracking system without a magnetic field, an unweighted straight line fit is generally a suitable description. The fit function, which represents a point $\mathbf{x}$ on a straight line, can be defined using the classical equation of a line in three-dimensional space:

$$\mathbf{x} = \mathbf{a}_1 + t \cdot \mathbf{a}_2, \tag{3.16}$$

where $\mathbf{a}_1$ is the state vector and $\mathbf{a}_2$ the direction vector.
When operating in Cartesian coordinates with the x, y and z-axes, defining the fit function in terms of the z coordinate can be advantageous in practice. To facilitate this, the state and direction vectors are modified accordingly. The state vector is constructed within the (x, y)-plane, ensuring that its z component is set to zero. On the other hand, the direction vector is normalised to adjust proportionally with the z position, resulting in a z component value of one. Consequently, equation 3.17 reads as follows:

$$\begin{pmatrix} x \\ y \\ z \end{pmatrix} = \begin{pmatrix} a_{1,\mathrm{x}} \\ a_{1,\mathrm{y}} \\ 0 \end{pmatrix} + z \cdot \begin{pmatrix} a_{2,\mathrm{x}} \\ a_{2,\mathrm{y}} \\ 1 \end{pmatrix}. \tag{3.17}$$

Fitting the trajectory through the measured points consists in determining the parameters of the chosen functional (e.g. equation 3.17) via minimisation of the χ^2. Since the χ^2 is additive, it is more convenient to decompose the three-dimensional problem into two two-dimensional ones. This approach simplifies the calculation and allows for a more straightforward analysis. Therewith, χ^2 for N measurements formulates as follows:

$$\chi^2 = \sum_{\mathrm{i}=1}^{N} \left(\frac{(m_{\mathrm{i,x}} - (a_{1,\mathrm{x}} + z_{\mathrm{i}} \cdot a_{2,\mathrm{x}}))^2}{{\sigma_{\mathrm{i,x}}}^2} + \frac{(m_{\mathrm{i,y}} - (a_{1,\mathrm{y}} + z_{\mathrm{i}} \cdot a_{2,\mathrm{y}}))^2}{{\sigma_{\mathrm{i,y}}}^2} \right). \tag{3.18}$$

Hereby, $m_{\mathrm{i}} = (m_{\mathrm{i,x}}, m_{\mathrm{i,y}}, z_{\mathrm{i}})^{\mathrm{T}}$ contains the measurement with its uncertainties $\sigma_{\mathrm{i,x}}$ and $\sigma_{\mathrm{i,y}}$. Calculating the derivatives of equation 3.18 with respect to the fit parameters a_1 and a_2 and setting them to zero provides the best estimate for the fit trajectory.
This model guarantees an analytical outcome, a fast implementation and robustness against falsely included measurement points. On the contrary, it is not suitable for representing low-momentum particles since their trajectories are characterised by multiple changes in direction rather than a straight line [23].

3.3.2 Weighted straight line

Massive low momentum particles in a tracking setup do not follow a straight line trajectory. The electromagnetic interactions in the matter, namely multiple scattering which is inverse proportional to the momentum, leads to deflections of the charged particle from its initial path. There are different approaches to account for this in a track model.
One way to include multiple scattering is demonstrated by the fit model of a weighted straight line. In this approach the fitted trajectory remains a straight line, as it represents the most likely path for the particle, considering that the average value of the multiple scattering angle is zero. However, the covariance matrices of the measurements are adjusted. The measurements, with respect to the initial straight trajectory of the particle, can be described with an offset arising from the detector and the scattering angle. Both offsets have a mean value of zero. While the measurement uncertainty is independent, the deviation caused by multiple scattering accumulates across the detector planes.
A simplified example can illustrate this concept: Suppose there is a particle that undergoes deflection due to multiple scattering on the first detector plane, causing it to deviate from its initial path. If there is no additional deviation on the second plane, the scattering angle at this point is zero. Nevertheless, the measurement obtained from the third plane deviates from the particle's initial trajectory due to the change in direction that occurred on the first plane. This indicates that the measurement on the third plane was influenced by the scattering that occurred on the first plane.
Using a weighted straight line fit implies that the measurement points are correlated across the telescope. The distribution of the individual scattering angles stays independent, but the deviation to the initial path can increase as more scatterers are encountered along the particle's trajectory. Figure 3.6 demonstrates the effect of this trajectory change.
The following formulas are used to describe two-dimensional measurements, as the three-

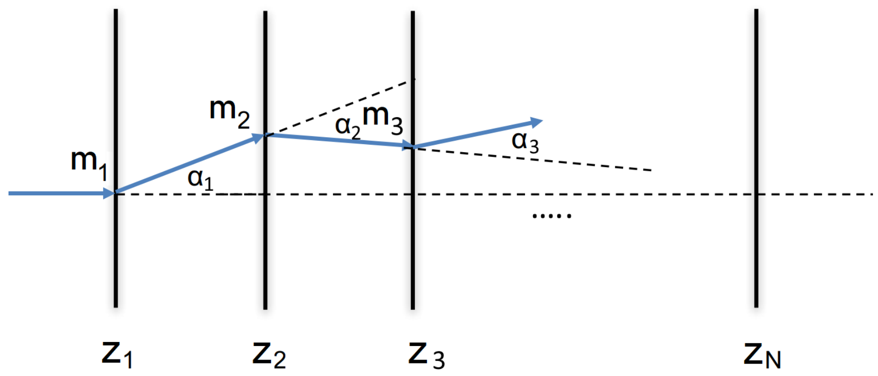

Figure 3.6: The figure, adapted from [14], shows the change of a particle trajectory throughout a tracking telescope due to multiple scattering. m represent the measurement points, α the scattering angles and z the positions of the planes on the z-axis.

dimensional measurement (x, y, z) can be projected independently into two two-dimensional ones (x, z) and (y, z). When m_i is the x or y component of a two-dimensional measurement point on the i-th plane of the telescope, the associated covariance for the measurement on any other plane j is

$$V_\mathrm{ij} = {\sigma_\mathrm{i}}^2 \delta_\mathrm{ij} + \sum_{\mathrm{k}=1}^{\mathrm{Min[i,j]}} \theta_{0,\mathrm{k}}^2 (z_\mathrm{i} - z_\mathrm{k})(z_\mathrm{j} - z_\mathrm{k}). \tag{3.19}$$

σ_i is the detector resolution of plane i, $\theta_{0,\mathrm{k}}$ is the standard deviation of the multiple scattering angle that can be calculated with equation 2.3 for the k-th scatterer and z is the distance to the respective plane. A short derivation for this non diagonal covariance matrix can be found in [14]. The first term represents the standard uncertainty that arises from the detector resolution, while the second term represents the uncertainty and correlation resulting from multiple scattering. Due to the lever arm, the uncertainties coming from multiple scattering increase as the distance between the planes becomes greater.

Several simplifications can typically be made. Firstly, the detector planes usually have an identical material budget, resulting in their contribution to multiple scattering being uniform. Secondly, the planes can be approximated as equidistant from each other.

The best fit parameters are obtained by minimising the χ^2-value. Since the uncertainties are correlated, the sum contains not only residual components from each individual plane but also mixed components:

$$\chi^2 = \sum_{\mathrm{i}=1}^{N} \sum_{\mathrm{j}=1}^{N} \left[m_\mathrm{i} - (a_1 + a_2 z_\mathrm{i})\right] V_\mathrm{ij}^{-1} \left[m_\mathrm{j} - (a_1 + a_2 z_\mathrm{j})\right]. \tag{3.20}$$

This formula follows equation 3.4 with x_m being given by the straight line fit function defined in equation 3.17. In matrix form, the chi-squared can be expressed as follows:

$$\chi^2 = (\mathbf{m} - \mathbf{Ga})^T \mathbf{V}^{-1} (\mathbf{m} - \mathbf{Ga}) \tag{3.21}$$

with $\mathbf{Ga}$ defining the fit function evaluated at the z coordinate of the measurement point

$$\mathbf{Ga} = \begin{pmatrix} 1 & z_1 \\ 1 & z_2 \\ 1 & z_3 \\ \vdots & \vdots \\ 1 & z_N \end{pmatrix} \begin{pmatrix} a_1 \\ a_2 \end{pmatrix}. \tag{3.22}$$

Now, χ^2 can be minimised by solving the following equations

$$\partial\chi^2/\partial a_1 = 0, \qquad \partial\chi^2/\partial a_2 = 0. \tag{3.23}$$

The outcome for the fit parameters is

$$\mathbf{a} = (\mathbf{G}^T\mathbf{V}^{-1}\mathbf{G})^{-1}\mathbf{G}^T\mathbf{V}^{-1}\mathbf{m}. \tag{3.24}$$

3.3.3 General Broken Lines (GBL)

As demonstrated in the previous section 3.3.2, global methods can take multiple scattering into account by incorporating additional uncertainties and correlations to the measurement. Moreover, an unweighted fit with scattering angles as additional fit parameters can be done. Both methods require computing time in the order of $O(N^3)$ with N being the number of measurements or scatterers [25]. They are easily outperformed by the fast local Kalman method, which has a linear computing time $O(N)$. In the following, a global fit model is presented, that considers multiple scattering and has a similar time complexity to the local Kalman filter, exploiting the sparsity of the matrix that represents the system of linear equations.

The General Broken Lines (GBL) formalism, developed at DESY Deutsches Elektronen Synchrotron, is a global and fast fit model for tracking particles affected by multiple scattering [25]. It achieves a computing time in the same order as the Kalman filter by incorporating the description of multiple scattering into an initial trajectory. The tracking method is not only able to account for the direction changes of a charged particle in matter, but also considers the energy loss in the material and, if present, any existing homogeneous magnetic field, all while determining the covariance matrix of all track pa-

rameters.
As the name implies, the fit model of the GBL formalism represents a broken line trajectory. The changes in direction along the trajectory are coming from multiple scattering within the materials. The angle between an initial track and the following scattered track is called kink. At first, it is tempting to imagine that with a broken line the track points can be perfectly matched to the measurement points. The magnitude of the kinks, however, is not arbitrary. They impose additional constraints on the track fit, similar to the measurements. In particular, the kinks are modelled to align with the multiple scattering expectation. This implies following a Gaussian distribution centred around zero with a standard deviation θ_0 calculated using equation 2.3. Consequently, the kinks are not treated as fit parameters but rather as process noise in the trajectory, which is compared to the expected value of zero.
The scatterings happen in matter like the detector material, but also in air which is present throughout the tracking telescope. To simplify the calculation while still keeping the model as truthful as possible, the extended material is approximated by several thin scatterers with an adapted radiation length. Herewith the number of fit parameters is kept small and an integration over the thickness of the air is avoided. This remodelling is portrayed in figure 3.7.

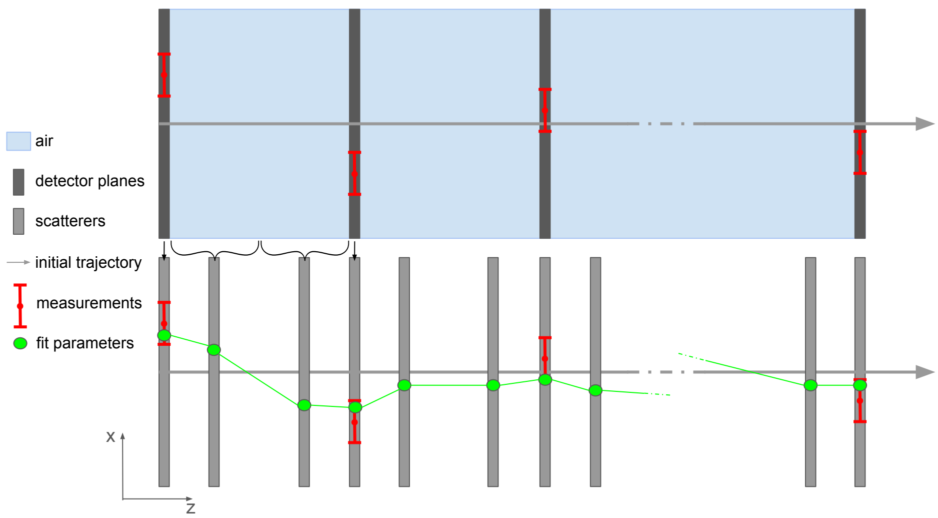

Figure 3.7: The upper part of the sketch depicts the true setup of a tracking detector with the detector planes, air in between the planes and the measurement points. The initial trajectory originates from an external or internal seed and is later broken apart to include multiple scattering. The lower sketch shows the actual implementation of the setup for the tracking algorithm. So called thick scatterers like the air are split into several thin scatterers. After all, the green line shows the final fit. To fully describe the new path without a magnetic field, only the intersection points with the scatterers are necessary. With a magnetic field the momentum is additionally needed to specify the curvature of the trajectories.

The broken lines algorithm is built up on an initial trajectory, that can come from a simplified fit of the measurements (an internal seed). If available, it can also be externally seeded using information from another detector.
GBL uses the minimisation of the chi-square to obtain the best fit parameters. However, prior to constructing the chi-square, it is necessary to define the residuals, their covariance, and the fit parameters. These definitions are performed in various coordinate systems to align with their respective properties. In most scenarios, a coordinate system is selected where the covariance matrix is diagonal, allowing for easier handling and interpretation of the data.
In the subsequent section, the particular coordinates are introduced. Afterwards, the parameters and residuals are discussed, leading to the final assembly of the chi-square.

Local coordinate systems

Apart from the global Cartesian frame (x, y, z), GBL uses local coordinate systems that match the studied quantities. At each scatterer a coordinate system (u, v, w) is defined. The base vectors $\mathbf{e}_u$ and $\mathbf{e}_v$ lie within the plane of the scatterer. $\mathbf{e}_w$ is chosen to be perpendicular to the plane when describing a measurement and parallel to the track direction when describing a kink. Additionally, there is the curvilinear system $(x_\perp, y_\perp, z_\perp)$ which is locally following the track with $\mathbf{e}_{x_\perp}$ or $\mathbf{e}_{y_\perp}$ in the global (x, y)-plane and $\mathbf{e}_{z_\perp}$ in the track direction. If no magnetic field is present the curvilinear system is simply the orthonormal system to the track with $\mathbf{e}_{z_\perp}$ pointing into the global track direction. The scatterer system and the curvilinear system changes track by track and scatterer by scatterer. All coordinate systems are depicted in figure 3.8.

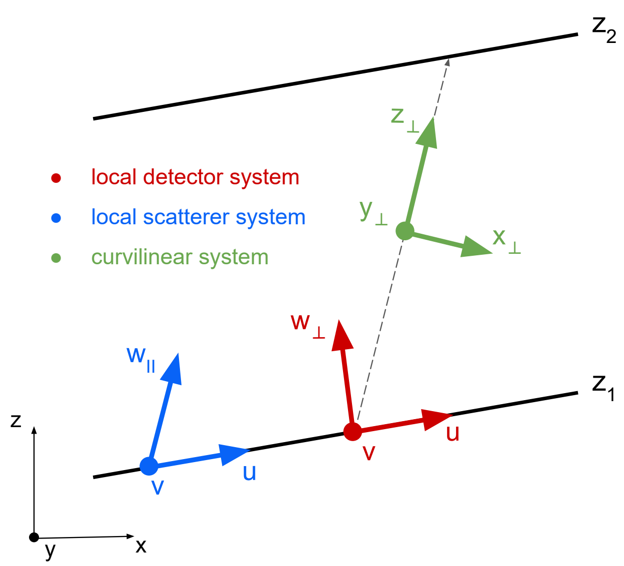

Figure 3.8: The sketch shows two rotated tracking planes z_1 and z_2. The trajectory is depicted as a dotted arrow pointing from one plane to another. It is a straight line if there is no magnetic field present. The green coordinate system represents the curvilinear frame. $\mathbf{e}_{y_\perp}$ shall be perpendicular to $\mathbf{e}_{z_\perp}$ and $\mathbf{e}_z$. Therefore it is pointing outside of the plane. $\mathbf{e}_{x_\perp}$ must be perpendicular to $\mathbf{e}_{y_\perp}$ and $\mathbf{e}_{z_\perp}$. The red coordinates represent the detector system and the blue coordinates represent the scatterer system. The origin of the local coordinate systems can be arbitrarily chosen on the plane and does not need to coincide with this representation.

Fit parameters

In the standard Cartesian coordinate system (x, y, z) the trajectory of a charged particle (with a homogeneous magnetic field in the y direction) is a helix. It can globally be described with a five dimensional vector. This is the most general case and it simplifies if there is no magnetic field like in this thesis. Nevertheless, in GBL, the parameters of a helix are always in effect since it includes all cases. The global parameters are

$$(q/p, \Phi, d, \lambda, y). \tag{3.25}$$

Hereby, the q/p term includes the effects of charge and momentum of the particle and describes the curvature of the helix. It describes the curvature of the helix. Φ is the angle at the distance d to the point of closest approach (PCA) in the (x, z)-plane. At this point d is minimal. Finally, λ is the dip angle to that plane and y is the offset at the point of closest approach. A visualisation of the global parameters in Cartesian coordinates can be found in figure 3.9.

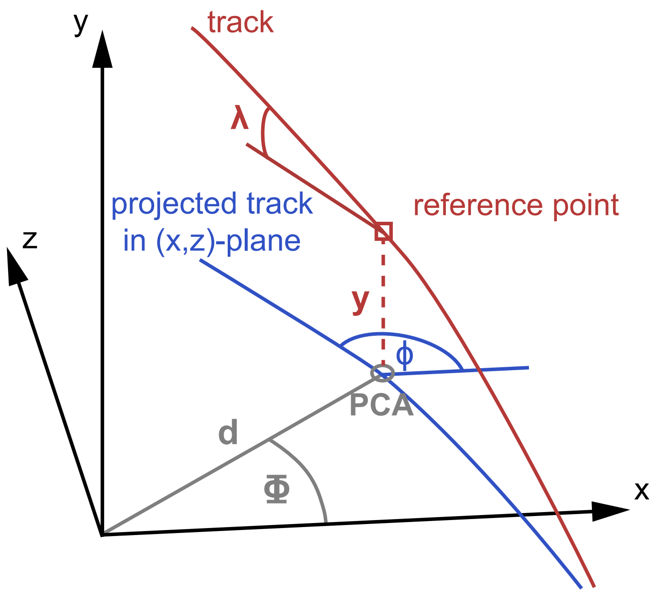

Figure 3.9: The figure shows the global track parametrisation of a helix according to equation 3.25. A helix trajectory is projected in the (x, z)-plane. The Point of closest approach (PCA) in this plane is given by the angle Φ and the distance d. The tangent at the reference point is provided by the angles ϕ and λ, where ϕ is the angle of the projected tangent to the x-axis and λ states the angle of the tangent at the reference point to the (x, z)-plane.

The fit parameters can also be described in the local system, namely the local detector system and the curvilinear system [19]. This consideration becomes important in the implementation of the General Broken Lines formalism for a specific tracking setup, as well as for non-iterative alignment methods like Millepede [12]. In the local detector system of a scatterer i, a track segment $\mathbf{s}_{\mathrm{locDec,i}}$ can be characterised by

$$\mathbf{s}_{\mathrm{locDec,i}} = (q/p_{\mathrm{i}}, u'_{\mathrm{i}}, v'_{\mathrm{i}}, u_{\mathrm{i}}, v_{\mathrm{i}}). \tag{3.26}$$

(u_i, v_i) is an offset that states the track intersection point on the detector plane and $(u'_\text{i}, v'_\text{i}) = \frac{\partial(u_\text{i}, v_\text{i})}{\partial w_{\perp,\text{i}}}$ is a slope describing the local track direction (tangent). A sketch is depicted in figure 3.10a.
In the curvilinear system a track is locally described by

$$\mathbf{s}_{\text{locCurv,i}} = (q/p_\text{i}, \lambda_\text{i}, \phi_\text{i}, x_{\perp,\text{i}}, y_{\perp,\text{i}}). \tag{3.27}$$

The curvilinear parameters are build in a hybrid local/global reference frame. The variables λ and ϕ are defined at the reference point and are able to describe the tangent at this point on the trajectory. However, the values of these variables are measured in the global Cartesian coordinate system. This is because they are mandatory to describe the curvilinear system since $z_\perp$ is in the direction of the tangent. Where λ is already defined by the global parameters, ϕ is defined as the azimuth angle of the projected tangent in the (x, z)-plane. Both parameters are depicted in figure 3.9.
$x_\perp$ and $y_\perp$ are the offsets similar to u and v but in the direction of the curvilinear base vectors. They are sketched in figure 3.10b. The Jacobians to transform the parameters from one system into a different local system are discussed in [39].

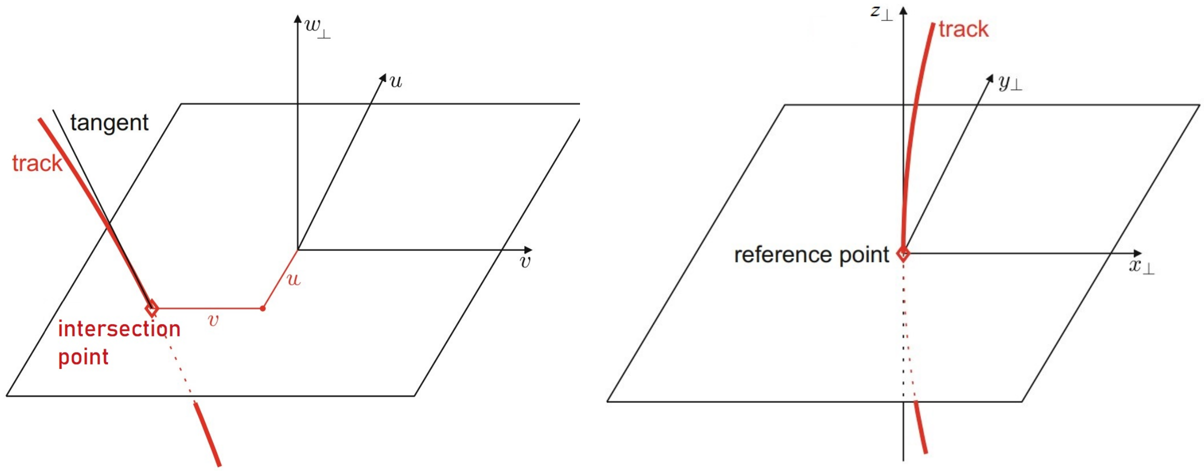

(a) (b)

Figure 3.10: (a) depicts the track parametrisation as per equation 3.26 [19]. The tangent of the track is described by the derivatives of u and v with respect to $w_\perp$. The reference point in the detector system corresponds to the intersection point of the trajectory with the plane. On the other hand, (b) displays the track parametrisation following equation 3.27. At the reference point, the tangent aligns with the $z_\perp$ direction.

From a global perspective only the offsets and the momentum of the local frames are necessary to fully describe all the trajectories in between the scatterers. The slopes or tangents can be calculated with the adjacent track points. Therefore, the fit parameter array $\mathbf{s}$ for a tracking telescope with n_{scat} scatterers is formed as follows:

$$\mathbf{s} = (q/p, \mathbf{u}_1, \mathbf{u}_2, ..., \mathbf{u}_{n_{\mathrm{scat}}}). \tag{3.28}$$

The local offset parameters can either be built in the detector system $\mathbf{u}_{\mathrm{i}} = (u_{\mathrm{i}}, v_{\mathrm{i}})$ or the curvilinear system $\mathbf{u}_{\mathrm{i}} = (x_{\perp,\mathrm{i}}, y_{\perp,\mathrm{i}})$ at the scatterer. The vector $\mathbf{s}$ includes all fit parameters that are later varied for the chi-square minimisation.

Residuals

In the GBL method the measurement point $\mathbf{m}_{\mathrm{i}}$ of a detector plane i is stated as a residual $\mathbf{r}_{\mathrm{m,i}}$ to the initial trajectory. The residuals are build in the local detector system (u, v). In these coordinates, the corresponding covariance matrix $\mathbf{V}_{\mathrm{m,i}}$ is diagonal. It contains the squared detector resolution in two directions u and v on the diagonal. The residual, representing the distance between the intersection point $\mathbf{x}_{\mathrm{i}}$ of a track and the measurement on a detector plane $\mathbf{m}_i = (m_{u,\mathrm{i}}, m_{v,\mathrm{i}})^{\mathrm{T}}$, is

$$\mathbf{r}_{\mathrm{m,i}} = \mathbf{H}_{\mathrm{m,i}}\mathbf{s} - \mathbf{m}_{\mathrm{i}} \tag{3.29}$$

The matrix $\mathbf{H}_{\mathrm{m,i}}$ multiplied with the fit parameter vector calculates the track intersection point with the detector plane in local coordinates.
In order to express detector related parameters (e.g. the residuals) in the curvilinear coordinate systems the projection matrix $\mathbf{P} = \frac{(x_\perp, y_\perp)}{(u,v)}$ is used. It transforms between the local detector coordinates and curvilinear system.
Since the kinks $\mathbf{k}$ are also variables in the fit parameter estimation, one additional residual needs to be formed. In GBL the kink angles are calculated in the local system of the scatterer. These coordinates are not optimal, as the covariance matrix of the kinks is diagonal in the curvilinear system, aligning with the principles of multiple scattering theory. In this system, the angle deflection in the two perpendicular directions to the track direction is uncorrelated. Thus, the covariance matrix can be represented as $\mathbf{V}_{k,\perp} = \begin{pmatrix} \theta_0^2 & 0 \\ 0 & \theta_0^2 \end{pmatrix}$, where each diagonal entry corresponds to the squared multiple scattering angle obtained from equation 2.3. Nevertheless, the covariance matrix can be easily transformed to the local system. With $c_1 = \mathbf{e}_{z_\perp}\mathbf{e}_u$ and $c_2 = \mathbf{e}_{z_\perp}\mathbf{e}_v$ being the projections of the offset directions onto the track direction, the covariance matrix in the local system can be calculated like:

$$\mathbf{V}_{\mathrm{k}} = \frac{\partial(u', v')}{\partial(x'_\perp, y'_\perp)} \begin{pmatrix} \theta_0^2 & 0 \\ 0 & \theta_0^2 \end{pmatrix} \left[\frac{\partial(u', v')}{\partial(x'_\perp, y'_\perp)}\right]^T = \frac{\theta_0^2}{(1 - c_1^2 - c_2^2)^2} \begin{pmatrix} 1 - c_2^2 & c_1 c_2 \\ c_1 c_2 & 1 - c_1^2 \end{pmatrix}. \tag{3.30}$$

To calculate the scattering residual, the kink angle in the local plane is calculated by multiplying the matrix $\mathbf{H}_{\mathrm{k}}$ with the parameter vector $\mathbf{s}$. The kink residual $\mathbf{r}_{\mathrm{k,i}}$ for the respective plane i then is formed as follows

$$\mathbf{r}_{\mathrm{k,i}} = \mathbf{H}_{\mathrm{k,i}}\mathbf{s} - 0 = \mathbf{H}_{\mathrm{k,i}}\mathbf{s}. \tag{3.31}$$

Whereas the expected value for the track point is the measurement point ($\langle \mathbf{H}_m \mathbf{s} \rangle = \mathbf{m}$), the expected value for the kink is zero ($\langle \mathbf{H}_k \mathbf{s} \rangle = 0$). Therefore the scattering residual is the kink angle itself.

Chi-square

The General Broken Lines formalism is a global minimum chi-square method, thus the fit parameters are determined by minimising:

$$\chi^2 = \sum_{\mathrm{i}=1}^{n_{\mathrm{meas}}} \mathbf{r}_{\mathrm{m,i}}^{\mathrm{T}} \mathbf{V}_{\mathrm{m,i}}^{-1} \mathbf{r}_{\mathrm{m,i}} + \sum_{\mathrm{i}=2}^{n_{\mathrm{scat}}-1} \mathbf{r}_{\mathrm{k,i}}^{\mathrm{T}} \mathbf{V}_{\mathrm{k,i}}^{-1} \mathbf{r}_{\mathrm{k,i}} \tag{3.32}$$

where the first sum arises from the measurements and the second from the kinks. The degree of freedom is

$$\begin{aligned} \nu &= 2((\mathrm{n}_{\mathrm{meas}} + (\mathrm{n}_{\mathrm{scat}} - 2)) - \mathrm{n}_{\mathrm{scat}}) \\ &= 2(\mathrm{n}_{\mathrm{meas}} - 2). \end{aligned} \tag{3.33}$$

This can be associated with the normal calculation for the degree of freedom (number of measurements - number of fit parameters). The total number of measurements includes both the measurements from the detectors $\mathrm{n}_{\mathrm{meas}}$ and the kinks $\mathrm{n}_{\mathrm{scat}} - 2$. There are two fewer kinks than scattering planes, as the first and last planes are not constrained on both sides. The number of required fit parameters is determined by the number of scattering planes $\mathrm{n}_{\mathrm{scat}}$. For three-dimensional measurements, this count is multiplied by two, as each measurement or scattering plane has two residuals, one in each dimension (u and v).
The minimisation of the chi-square leads to a linear equation system $\mathbf{A}\mathbf{s} = \mathbf{b}$:

$$\mathbf{A} = \sum_{\mathrm{i}=1}^{\mathrm{n}_{\mathrm{meas}}} \mathbf{H}_{\mathrm{m,i}}^{\mathrm{T}} \mathbf{V}_{\mathrm{m,i}}^{-1} \mathbf{H}_{\mathrm{m,i}} + \sum_{i=2}^{\mathrm{n}_{\mathrm{scat}-1}} \mathbf{H}_{\mathrm{k,i}}^{\mathrm{T}} \mathbf{V}_{\mathrm{k,i}}^{-1} \mathbf{H}_{\mathrm{k,i}} \tag{3.34}$$

$$\mathbf{b} = \sum_{\mathrm{i}=1}^{\mathrm{n}_{\mathrm{meas}}} \mathbf{H}_{\mathrm{m,i}}^{\mathrm{T}} \mathbf{V}_{m,i}^{-1} \mathbf{m}_{\mathrm{i}} - \sum_{i=2}^{\mathrm{n}_{\mathrm{scat}-1}} \mathbf{H}_{\mathrm{k,i}}^{\mathrm{T}} \mathbf{V}_{\mathrm{k,i}}^{-1} \mathbf{k}_{\mathrm{i}}. \tag{3.35}$$

To solve the equation system for $\mathbf{s}$, $\mathbf{A}$ has to be inverted. The matrix has a special form which allows the usage of the root-free Cholesky decomposition [20]. As a result, the inversion of $\mathbf{A}$ and thus the calculation of $\mathbf{s}$ are possible with a computing time in the order $O(n_{\text{scat}})$. This makes the GBL formalism perform faster than other global methods.

Procedure

The implementation of a given tracking setup with measurements starts with the definition of the seed trajectory. It is defined in the local system and gives information about the whole tracking telescope and its measurements.
First, each track point of the initial trajectory is constructed with the Jacobian

$$\mathbf{T}_{\text{i}} = \partial \mathbf{s}_{\text{locCurv,i+1}} / \partial \mathbf{s}_{\text{locCurv,i}} \tag{3.36}$$

which states the transformation of the local track parameters from plane to plane. As the curvilinear system is a track following frame, the Jacobian is simply a transport within the curvilinear frame to the destination plane. At each plane, the measurements and kinks have to be defined. Usually the kinks of the initial trajectory are zero. The measurements are incorporated as residuals to the initial trajectory in the local detector system.
Now, the chi-square can be constructed and derived. This brings up a linear equation system. By decomposing the matrices, a fast inversion is possible and results in the solution with the best fit parameters.

The goal of this chapter was to present different methods for global and local track fitting. In the beginning the tools for a successful parameter estimation were given. The considerations have show that the minimisation of the chi-square is a fundamental concept for the particle track reconstruction.
The chapter introduced various models and provided explanations of their underlying concepts. These discussions establish a foundation for future investigations into specific tracking setups and their practical implementations. It should be noted that the global methods differ in terms of their complexity, accuracy, and computational requirements. This differentiation highlights the importance of carefully selecting the appropriate method based on the specific tracking scenario and available computational resources.

Chapter 4

TRACKING WITH AN ALPIDE TELESCOPE

This chapter will cover an experimental application, where global track models were used to reconstruct particles that passed a tracking setup.
Following the recent upgrade of the ITS in ALICE, the tracking detector is now fully digital, leading to the loss of previously available analogue information about the energy loss of traversing particles. Currently, investigations are performed to study the possibility of regaining this information through the analysis of the cluster size of incoming particles on the ALPIDE chip.
In order to study the cluster size dependencies, several testbeams were conducted using various particle species. Testbeams serve as complementary measurements to laboratory characterisations of sensors and are commonly used to investigate parameters of interest such as efficiency, spatial and timing resolution, and the influence of radiation damage, among others. The properties of the particle beam are well-known and can be adjusted and optimised for specific research purposes.
This study focuses on particles with momentum below $1\,\mathrm{GeV}/c$. At these momenta particles are strongly affected by multiple scattering. Nonetheless, it is crucial to accurately track them to enable subsequent analysis. In such scenarios, global track models that incorporate the specific considerations for multiple scattering prove to be mandatory.
The data discussed in this study were obtained from a testbeam conducted in November 2022, with a low kinetic energy proton beam in the range of $80-200\,\mathrm{MeV}$. The setup and characteristics of the testbeam will be detailed in this chapter, followed by the application and performance evaluation of the introduced global tracking algorithms.
There is an established method for the analysis of sensors that involves high momentum, resulting in straight trajectories with little beam divergence. In this method, projectiles hit the surface of the sensors perpendicularly. This approach is necessary to characterise

new sensors and eliminate any unknowns. However, when attempting to apply this established method, unsatisfactory results were observed. As a result, this thesis investigates the alignment and track reconstruction of data from low momentum protons to address this issue.

4.1 Telescope characterisation

4.1.1 Testbeam facility

The data discussed in this study were collected during a testbeam conducted at the Centrum Cyklotronowe Bronowice, which serves as a proton therapy treatment centre in Krakow, Poland. Over the last decades irradiation with protons, or ions in general, became more and more relevant for cancer treatment.
The typical kinetic energy range for protons used in therapy is between 70 MeV and 250 MeV. This corresponds to a momentum range of 370 MeV/c to 730 MeV/c. To ensure precise irradiation of the cancerous tissue, a well collimated beam ($\sim$ mm) is essential. Furthermore, high particle rates (in the order of 10^{10} protons/s) are common [34].
Outside of normal working hours, most medical accelerator facilities offer the opportunity to access the particle beam for scientific purposes.

4.1.2 Setup

Due to the high rates, the telescope was positioned at an angle relative to the primary beam. In this context, a telescope refers to a group of individual sensors placed consecutively along the beam axis. A secondary beam was generated by directing the primary protons onto a 500 µm thick aluminium target, positioned 2 m behind the beam exit. The scattered protons within the acceptance of the setup (triggered by the coincidence of two scintillators) were further considered. Rates ranging from a few kHz to several tens of kHz were achieved. To adjust the rate and increase statistics per operating point, the setup was rotated at angles between $\alpha = 10 - 15\,^\circ$ with respect to point A, relative to the primary beam, until satisfactory particle rates were obtained. A sketch of the whole setup is presented in figure 4.1.
Each telescope plane consists out of an ALPIDE chip, that can be rotated around the y axis, offering the possibility to study tracks that impinge at angles between 0 (perpendicular to the sensor) and up to $70\,^\circ$. From now on, the planes will be counted starting from zero. From the testbeam data, a representative subset was chosen, with all ALPIDE sensors rotated by $30\,^\circ$ and evenly spaced at distances of 10.0 cm, which serves as case study for the tracking algorithms.

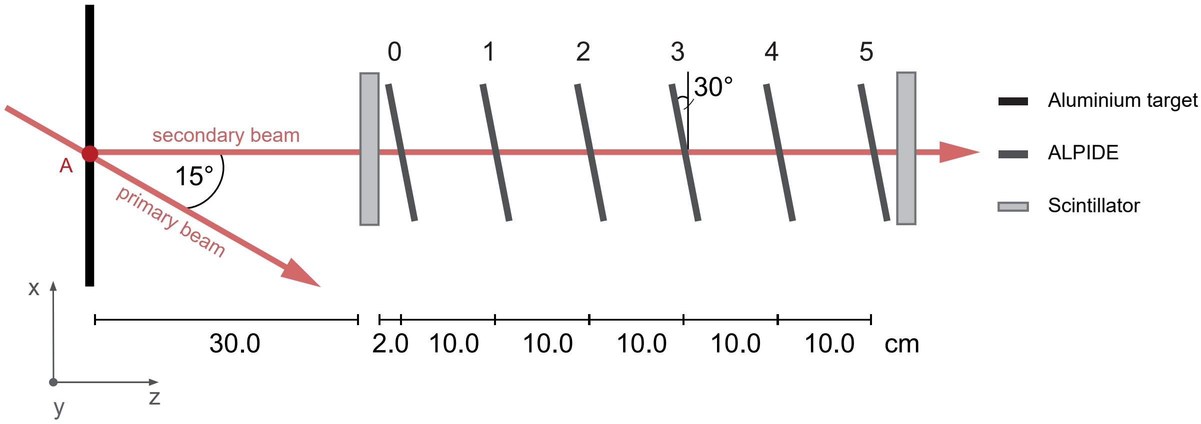

Figure 4.1: The sketch depicts the tracking setup in the x-z-plane (not to scale).

At the position of the target, the beam widens due to scattering with air molecules, resulting in an approximate diameter of 1 cm. With additional scattering in the target and the first scintillator, the particles disperse even further, spreading out with a wide range of inclination angles once they traverse the telescope.
For this data sample the kinetic energy of the beam was $E'_{\mathrm{kin}} = (120.0 \pm 0.8)\,\mathrm{MeV}$ at the beam exit. The energy spread is consider to be 0.7 % of the beam energy [31]. As the protons traverse material until they reach the first ALPIDE, their energy reduces. Table 4.1 shows the mean energy loss per path length $-\mathrm{d}E/\mathrm{d}x$, the density ρ, the thickness l of the traversed material and the total energy loss

$$\Delta E = -\mathrm{d}E/\mathrm{d}x \cdot \rho \cdot l. \tag{4.1}$$

material	$-\mathrm{d}E/\mathrm{d}x\,[\mathrm{MeVcm^2g^{-1}}]$	$\rho\,[\mathrm{g\,cm^{-3}}]$	$l\,[\mathrm{cm}]$	$\Delta E\,[\mathrm{MeV}]$
air until the target	5.615	0.001205	200	1.359
aluminium	4.996	2.699	0.05	0.676
air after the target	5.684	0.001205	30	0.002
EJ-200 plastic scintillator	6.376	1.032	1	6.719

Table 4.1: The table illustrates the parameters required for calculating the energy loss of the projectile protons from the beam exit to the tracking telescope. The values come from a calculation with the Catima library [35].

Eventually, the actual kinetic energy of the incoming particles is estimated to be $E_{\mathrm{kin}} = (111.3 \pm 0.9)\,\mathrm{MeV}$ at the first detector plane.

4.1.3 Alignment

The precision of the mechanical assembly of the detectors in any experiment is limited and therefore a software alignment is crucial. The testbeam setup mainly deviates from a perfect alignment due to translational and rotational degrees of freedom of the individual planes present due to the mechanics or due to the positioning of the sensors on the carrier cards, among others. Moreover, even through using for example precise laser alignment systems, the precision achieved is in the order of few hundred µm. In order to benefit from the intrinsic spatial resolution that the ALPIDE sensors have, an offline software alignment is mandatory, where their positions and orientations are determined with similar precision.
For systems like the ITS in ALICE, there are even more effects like torsion or surface deformation, which can occur over time, for example caused by gravitational effects or thermal expansion [21].
In the alignment process, the provisional geometric arrangement is updated with the true positions and rotations of the planes. Only the z coordinate of the detector position stays unchanged. After all, a small misalignment in the z position has no noteworthy impact on the tracking quality compared to a misalignment in x and y, as the following example demonstrates.
Imagining two detector planes with a distance of 2 cm to each other are traversed by a particle with a straight track, inclined 5° to the z-axis. If the second plane has a misalignment of 1 mm in x or y directions, the residual (the distance between hit position and track intercept on the plane) projected onto the plane will deviate by 1 mm. So, a small deviation in the x and y directions results in a shift of tens of pixels. However, if the misalignment is 1mm in z direction the projected residual r will only be

$$r = \tan 5^\circ \cdot 1\,\mathrm{mm} \approx 0.09\,\mathrm{mm},$$

which is only a few pixels. Similar arguments demonstrate that rotations around the x and y axes also have minimal impact.
The alignment is considered sufficient when a level of precision is achieved, such that the resolution of the reconstructed track is not significantly degraded by residual misalignments compared to the resolution expected in an ideal case [13]. In other words, the shifted mean of the residual distributions should be significantly smaller than the spatial track resolution of the telescope.
To fix coarse shift of the telescope planes, usually a so called prealignment is performed first. It does not require any tracking but instead utilises only the positions of the hits (or more precisely the centre of gravity of hits forming a cluster). By fixing one plane as a reference plane, the correlation between each hit position and the hit position on the

reference plane in the same event can be plotted. For straight, relativistic particles, a narrow peak at the position of the true plane shift is expected, as shown in figure 4.2. Hence, a coarse correction for the true displacement can be done in the software to shift the mean of the peak in the correlation to zero.

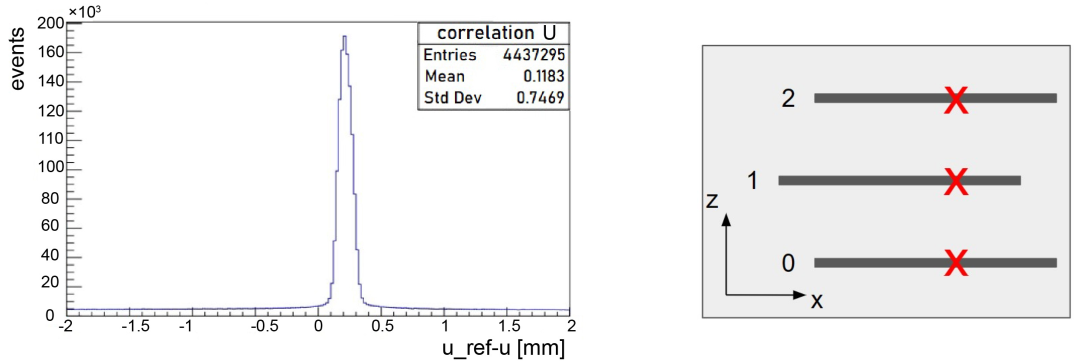

Figure 4.2: On the right, a schematic of a detector telescope with a slight misalignment of plane 1 is shown. A relativistic particle has passed the layers, perpendicular to their surface, and its hit positions are marked with red crosses. On the left, the correlation between the hit positions on plane 0, the reference plane, and plane 1 are drawn in local coordinates (u, v, w)[28]. A systematic shift is observed for the hits in plane 1, with respect to the reference plane, indicating the translational misalignment in the x direction.

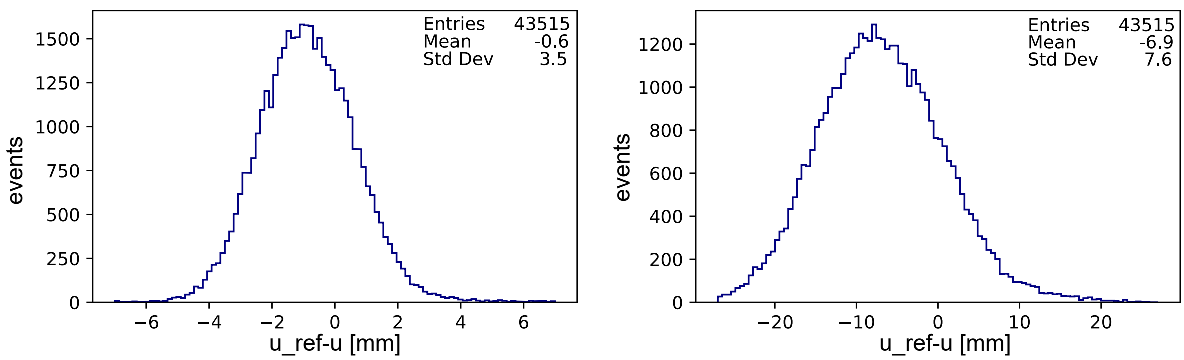

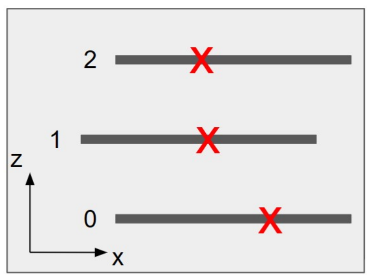

Figure 4.3: On the bottom right, a schematic of a detector telescope with a slight misalignment is shown. A low momentum particle has passed the planes and its hit positions are marked with red crosses. On the top, the correlations between the hit positions on plane 0 (the reference plane) and plane 1 (left plot), or respectively, plane 5 (right plot) are illustrated.

However, performing a prealignment is challenging under our conditions, dealing with low momentum particles and a divergent beam. As shown in figure 4.3, the previous assumptions are no longer valid because the initial trajectory may be inclined (because of the beam divergence) and it may no longer be straight in case of the probable multiple scattering in the detector planes. As a consequence, the distribution in the correlation plot is very broad and worsens with increasing distance from the reference plane as demonstrated in the right side of figure 4.3.

Apart from the broad correlation plots, there is another reason against the correlation-based prealignment method. The prealignment assumes that the particle beam has passed through the tracking telescope parallel to the z-axis. Only under this condition, a measure of the translational displacement in the respective axis is valid. If this assumption is not met, the prealignment will still shift the planes as if the beam was parallel to the z-axis. This behaviour is illustrated in figure 4.5. As a result, it will introduce a systematic shift of the planes in the direction opposite to the beam inclination. Ultimately, this new arrangement will not accurately represent the true positions of the detectors.

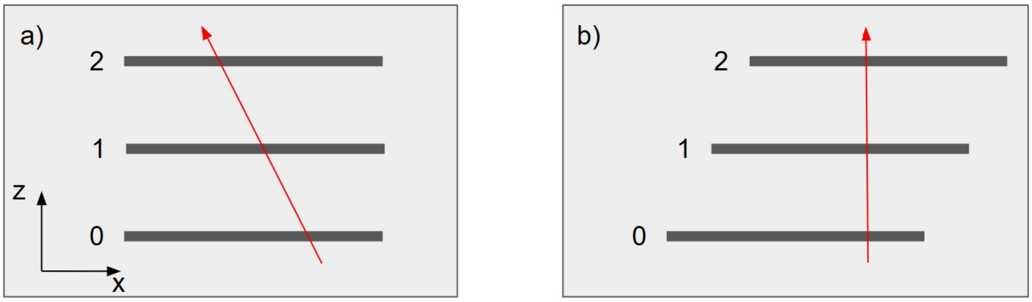

Figure 4.5: The sketch illustrates three detector planes. The red arrow represents the main beam direction. In a), a particle coming from the beam is depicted. In b), the correlation-based prealignment method was applied. Due to the inclination of the beam with respect to the z axis, the planes were systematically shifted to the right. As a consequence, the reconstructed particles primarily appear parallel to the z-axis. However, the positions of the planes do not correspond to the actual detector placements.

Instead of performing the prealignment, the alignment can directly be realised through a precise, iterative process that utilises histograms of the spatial residuals distribution from tracking to extract corrections for the plane positions. As such, at each iteration the mean value of the residual distribution is taken as the correction for the plane position and afterwards a new fit is performed.

In general, two degrees of freedom remain undefined in this procedure, namely a simultaneous shift and rotation of all planes. This means that the alignment can find two arrangements where the residuals are shifted to zero but only one of them agrees with the true detector positions. To restrict this shearing, one additional plane apart from the reference plane is fixed to keep the global x and y position of the detector at zero during the alignment procedure [12]. These two planes are expected to be carefully aligned externally. For the discussed tracking setup planes 0 and 2 were fixed.

Usually, the best fitting model is chosen for the track-based alignment. Under these circumstances however, a straight line was preferred instead of the better-fitting broken line algorithm. Only after the first alignment using a straight line fit is performed, the broken line fit is used for a second alignment. The reasoning behind this is that without the prealignment, the residual based alignment has to absorb the coarse shifts directly. If the mechanical alignment is not perfect, the broken line algorithm can fail to find the global minimum of the χ^2-equation.

In particular, the GBL fit falls into a local minimum. This means that a small variation of the plane position does not result in a possible improvement of the fits. Instead, the trajectories stay the same and, in this case, exhibit a residual distribution that is shifted closer towards zero but at the cost of the kink angles being strongly shifted from the physical expectation, i.e., the multiple scattering distribution. The distributions are shown in figure 4.6. The residual distributions give the impression of a successful alignment. However, the fits do not withstand the minimal possible χ^2-values, indicating that the true plane positions were not achieved.

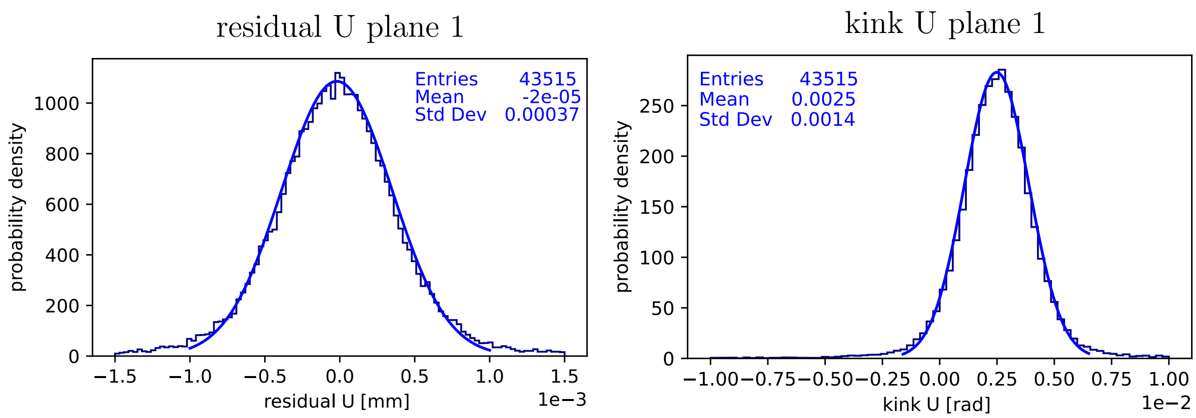

Figure 4.6: Output after the alignment was directly performed with a GBL fit. On the left, the residual distribution is depicted, centred around zero, indicative of an alignment that converged. On the right, the respective kink distribution is shown, exhibiting a mean significantly different from zero which was introduced by the alignment algorithm in order to minimise the width of the spatial residuals and to correct any shifts of its mean. The mean and standard deviation (Std Dev) are derived from a Gaussian fit illustrated in blue (inner 98 % core). The values were calculated in the local detector system, which has the coordinates (u, v, w).

A straight line fit does not have the freedom to shift the residuals to zero without acknowledging the true detector positions in the alignment procedure and therefore is more suitable to handle the coarse shifts. Figure 4.7 shows the residual distribution before and after the alignment with a straight line. As can be seen, the true displacement of the planes are identified by the shift of the mean of the residual distributions and corrected for.

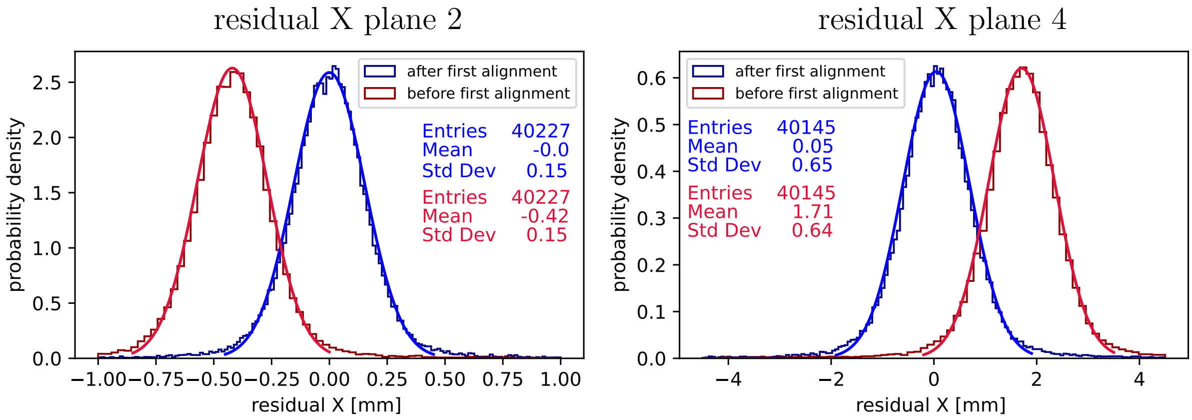

Figure 4.7: Distribution of residuals before and after the first alignment with a straight line fitted with a Gaussian. The final precision is not achieved yet. The width of the residuals increases with the plane number because a weighted straight line fit was used. This implies that the track intercept towards the end of the telescope, where the particle trajectory has been influenced by multiple scatterers, has a broader distribution.

By having a closer look at the means of the Gaussian fits applied on the residuals distributions, it is clear that the coarse shifts are now corrected. If the goal is to track the particles with a tracking precision of a weighted straight line, this alignment is sufficient. However, if a higher precision is desired, using General Broken Lines, a second alignment becomes necessary. This is because the residuals of the GBL fit with this alignment show significant deviations of the means from zero compared to the associated tracking resolution. Therefore, a second iteration is performed, this time using the broken line model to achieve a more precise alignment.

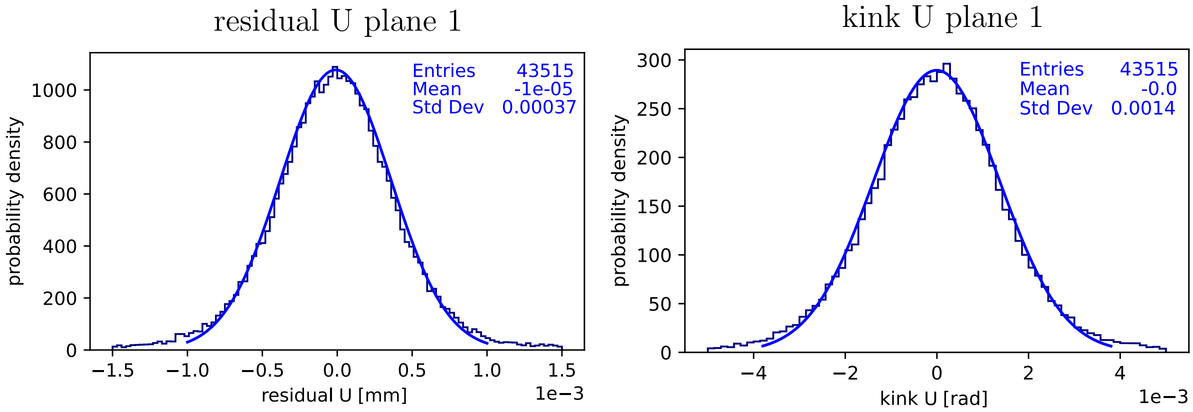

Figure 4.8: The residual and kink distribution from a General Broken Lines fit after the final alignment are depicted. The mean of the residual is two orders of magnitudes better than the tracking resolution (the tracking resolution is in the order of the spatial detector resolution), which means that the alignment was successful and satisfactory. The kink angle distribution is also centred around zero as expected from the multiple scattering theory.

Finally, a good alignment is achieved, resulting in very narrow distributions of residuals with means magnitudes below the tracking resolution and sensible kink angle distributions centred around zero as illustrated in figure 4.8.

Quality assurance using the Chi-square distribution

It is not always obvious to the naked eye whether the residuals are correctly distributed. Furthermore, checking every plane for the residuals and potential anomalies is not a convenient task. A straightforward and fast way to probe the alignment and the tracking quality is to compare the χ^2-distribution to its theoretical distribution. This can provide quick feedback on the tracking quality and reveal possible implementation mistakes. However, the cause of a potential deviation is not always clear.

In the following, different χ^2-distributions will be examined to provide an understanding of their characteristics when model parameters are incorrectly estimated. This includes a misalignment in the setup and a wrong uncertainty estimation. A discussion for the appearance of the chi-square distribution for different track models will be provided later in section 4.2.

The subsequent examples were obtained from a weighted straight line fit to the data of low momentum protons. The chi-square distributions are depicted in figure 4.9. First, only translational degrees of freedom were allowed in the alignment, but no rotational ones. The distribution of individual track χ^2s is shown in panel (a) and is compared to the expected χ^2-curve for ndof $= 8$ drawn in red. The distribution shows that a large amount of tracks have a good chi-square value. However, the entire distribution has a small shift to higher chi-square values compared to the expected probability density function[1].

There are also common fitting issues, such as the overestimation or underestimation of the uncertainties like the position resolution of a detector or the multiple scattering angle. This can be demonstrated by modifying fit example shown above. Rather than accurately accounting for the multiple scattering, the uncertainty for the scattering angle was artificially increased or decreased as an example. Consequently, the χ^2 changes its shape as shown in panels (b) and (c) of figure 4.9.

Usually, it is unlikely to incorrectly estimate well known uncertainties such as the one coming from multiple scattering or the spatial detector resolution. However, calculating the correct covariance matrix presents a challenge. Depending on the coordinate system in which the residual is constructed, the covariance matrix undergoes a change in form and may require a projection or transformation into the appropriate system. Consequently,

[1]Even with a perfect alignment the distribution disperses asymmetric around the pdf. There are too many track entries at high chi-square values. This is not a problem of the alignment but of the tracking model itself and will be discussed later in section 4.2.1 of this thesis.

the matrix is no longer diagonal. Failure to perform this transformation correctly results in either overestimation or underestimation of the uncertainties.

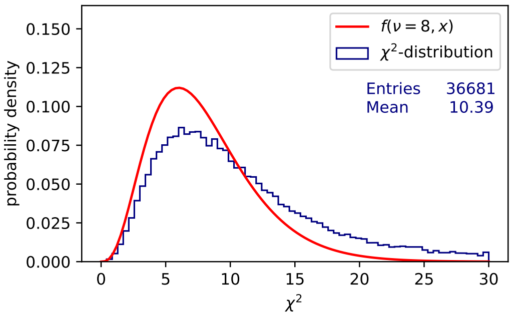

(a) Alignment without rotations

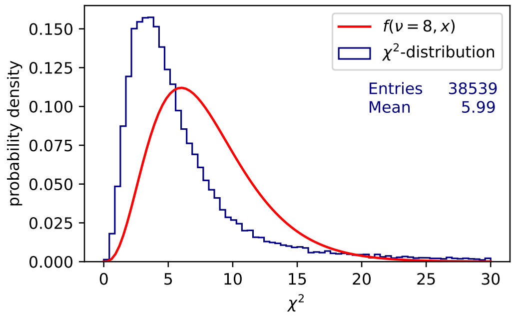

(b) Overestimation of the uncertainties

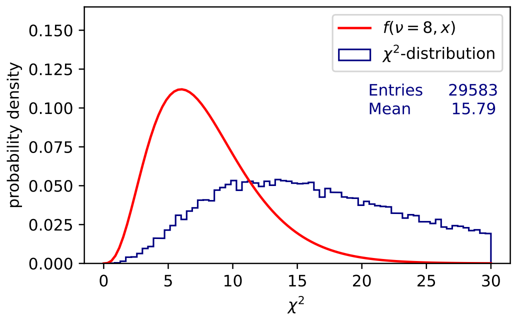

(c) Underestimation of the uncertainties

Figure 4.9: The figures illustrate different chi-square distributions for common fitting issues. Graph (a) shows the χ^2 if no rotations are considered in the alignment. (b) and (c) depict the χ^2-values if the uncertainties were over or under estimated, respectively. The red line indicates the expected distribution from the chi-square statistics stated in equation 3.3.

Overall, the examples demonstrate that it is not possible to unambiguously detect a problem in the tracking process simply from the distribution of the chi-square alone. Nonetheless, it is possible to interpret the χ^2 to gain a basic understanding of the fit and the alignment quality.

4.1.4 Filtering of events

Tracks reconstructed in a tracking telescope undergo several quality criteria before they are used for the final analysis. Typically, a selection on the chi-square values is employed. This is done to identify track patterns that may not have been generated by protons from the particle beam of the facility.

A second criterion that can be applied is to impose a restriction on the number of planes that must register a hit. Generally, fitting a trajectory requires more than two planes to be hit. Otherwise, the degree of freedom of the fit is zero which means that the parameter

of the trajectory are not free to vary, resulting in a meaningless fit. On the other hand, the greater the number of required planes, the higher the probability that the hits were genuinely produced by a projectile particle from the beam.
Subsequently, various characteristics of the telescope are discussed, along with the impact of quality restrictions such as the requirement on the number of planes registering a hit and the application of a chi-square selection.

2D correlation plots

The 2D correlation plot depicts the cluster position in the local coordinates u and v on the plane under consideration and the reference one. If the hits on each plane were produced by the same particle the graph should show a correlation. In the ideal case, all beam particles pass through the telescope perpendicular to the surface of the sensors and only in a small, targeted area. In that case the correlation plot would show narrow points along the diagonal line of the two axes. This line fades out below and above certain pixel values because the beam intersects the detector only in a small area.
In the studied data, the low momentum of the particles combined with the encountered material along the way, results in a wide particle beam with many different inclination angles around the direction perpendicular to the sensors. With these circumstances, the correlation plots exhibit an unusual and distinctive shape that will be explained in this section. However, the visualisation of the correlation can still, to some extent, indicate whether two hits in the telescope originate from the same source or were produced independently, as activity from the beam is expected to be systematic in all sensor planes.
The 2D correlation plot without any selection on the data is shown in figure 4.10a. Several selection criteria were imposed successively. The first step involved reducing the data to include solely events where less than two cluster were registered on each detector plane. A second cluster on the plane is primarily produced by delta electrons [22].
It is very profound to discard every event where there was at least one plane with two clusters. Especially if the number of available events is small, it can become important to avoid this strong selection. An alternative is to utilising the χ^2-value of a fit. This approach prevents discarding every event with two clusters on a plane and enables a distinction between the cluster produced by a projectile proton and other clusters. Hereby, every combination of clusters on different planes is tracked and the trajectory with the smallest chi-square value is considered to be the true path of the projectile particle. However, since there was sufficient statistical data available in this study, it was not mandatory to perform a fit and hence use the χ^2-value at this point of the selection.

The second restriction was to filter the data for events that have at least one cluster

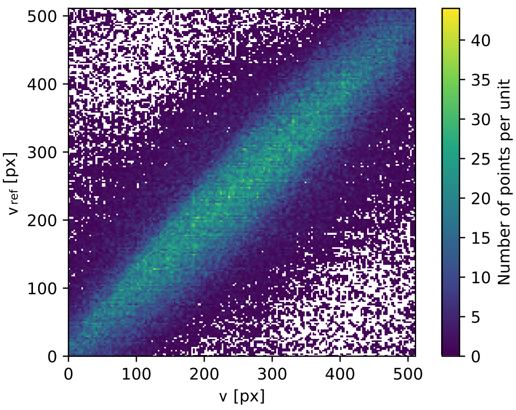

(a)

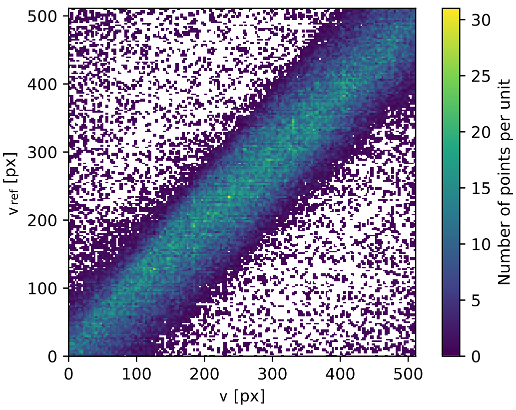

(b)

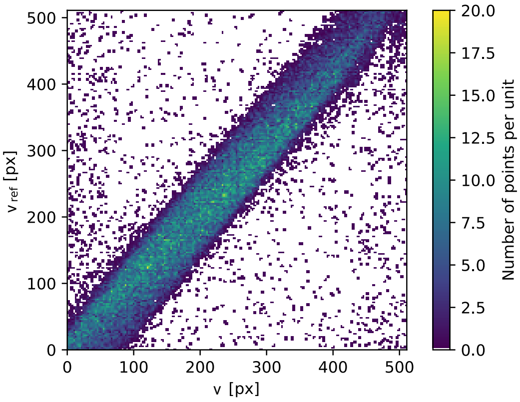

(c)

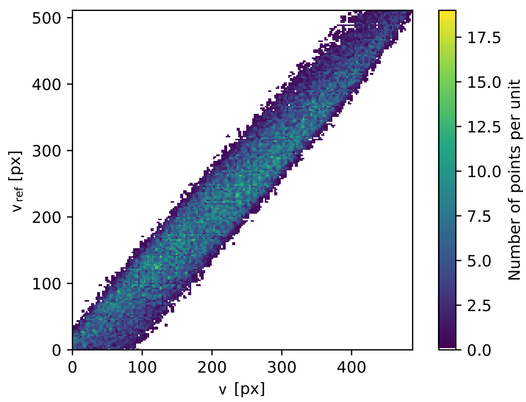

(d)

Figure 4.10: The figures show the V-correlations of plane 0 and plane 1. In (a) the correlation with no filter is depicted. (b) shows the correlation for events filtered for maximum one cluster on each detector. In (c) events were selected, where each detector plane has exactly one cluster. (d) depicts the correlation plot with the previous selection criteria and an additional χ^2 selection that was performed after tracking.

on every plane (6-plane events). Together with the earlier selection the remaining data solely includes events that have exactly one cluster on every plane.

After applying these filters that are independent of a track fit, the correlation plot already demonstrates an improvement in the removal of uncorrelated hit points. However, there are still events with clusters that were very unlikely to be produced by a traversing projectile particle. Therefore, the events are also filtered based on a chi-square selection. This finally rejects the remaining uncorrelated hits. The final correlation plot is shown in figure 4.10d.

The dispersion shows the same diagonal line as expected in the ideal case but stretched evenly over the whole sensor area. This behaviour is caused by particles penetrating the detector all over the plane and not just in a small region. Moreover, the diagonal line is broadened. This results from the different inclination angles of the protons.

The inclinations of the projectile particles give the dispersion a distinct appearance, as illustrated in figure 4.11a. The dotted red lines represent symmetric boundaries around the diagonal line, originating from inclined tracks. In fact, the distribution is not totally symmetric. For a low pixel number on the reference plane there are no hits found above the diagonal. For high pixel numbers, the exact opposite is the case.

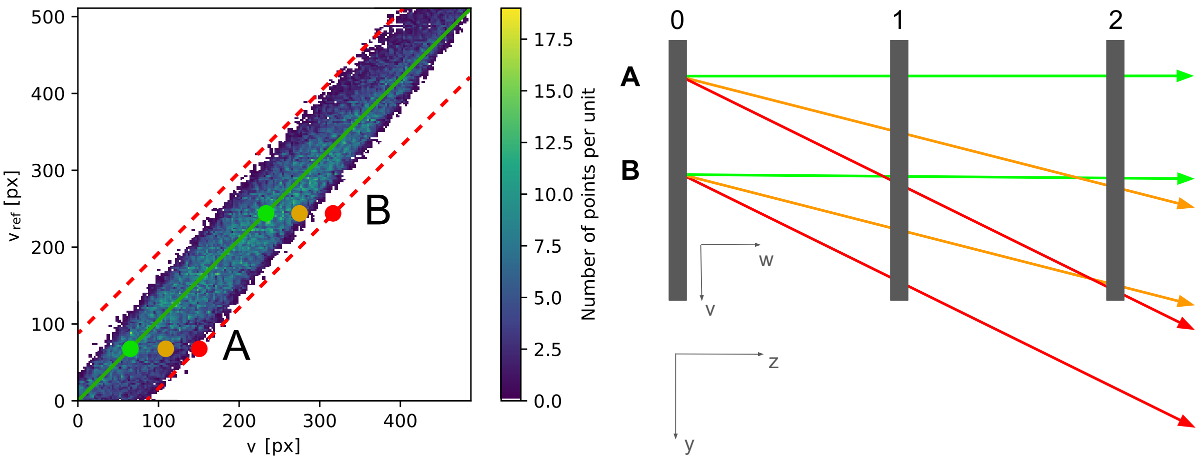

(a) (b)

Figure 4.11: (a) depicts the correlation plot of plane 0 and 1, considering all selection criteria. Additionally, a sketch is drawn to illustrate different areas of the correlation plot. The dotted line indicates the area where correlation points are expected at first glance. Below the diagonal, the correlation points originate from particles whose pixel numbers of the clusters increase throughout the telescope. Hence, the hit pixel number of the plane under consideration is larger than on the reference plane. Above the diagonal, the hit pixel numbers of the particles decrease throughout the telescope.
(b) shows a sketch of particle tracks passing through three telescope planes. The first plane represents the reference plane. In case A, all correlation points with the associated track inclination are visible in (a). The colours link the inclination of the particles to their location in the 2D correlation plot. For case B, particles with a stronger inclination (red) are not present in the correlation plot because they fall outside the acceptance of the telescope.

The expected symmetric distribution of the correlations around the central diagonal line misses hits in these regions due to the finite acceptance of the telescope. An exemplary look at tracks with an increasing hit pixel number throughout the telescope, can provide an insight. They are located below the diagonal in the correlation plot and are visualised in figure 4.11b.

Case A and B show the same inclined particles but with a different intersection point on the reference plane. Tracks that have a small pixel number on the reference plane (Case A) hit every plane in the exemplary telescope, even with strong inclinations. Tracks with the same strong inclination but a higher pixel number on the first plane (reference plane) are not covered by all telescope planes anymore. Consequently these track do not fulfil the requirement to hit all detector planes. Therefore, the entries below the diagonal are missing at high pixel numbers of the reference plane. Mirroring the example for tracks with the opposite inclination equivalently explains why entries above the intersecting line are missing at low pixel numbers.

Angular distribution of the particles

The primary beam initially contains protons with almost parallel trajectories to each other, narrowly confined in space. After the particles penetrate the material, especially the scintillator, their spatial distribution widens. Additionally, they are not parallel anymore but exhibit different inclination angles.
With a straight line fit, the inclination angle can be extracted after tracking. If the events were filtered for 6-plane events, the maximum possible inclination angle of a track is given by the acceptance of the telescope. The accepted angles in x and y are calculated as follows, where the active area of the ALPIDE measures $3 \times 1.38\,\text{cm}^2$ and the distance from the first to the last plane is $50\,\text{cm}$:

$$\alpha_{\text{X}} = \pm\tan^{-1}\left(\frac{3\,\text{cm}}{50\,\text{cm}}\right) = \pm 3.4\,^\circ \,\widehat{=}\, \pm\, 0.059\,\text{rad}$$

$$\alpha_{\text{Y}} = \pm\tan^{-1}\left(\frac{1.38\,\text{cm}}{50\,\text{cm}}\right) = \pm 1.58\,^\circ \,\widehat{=}\, \pm\, 0.028\,\text{rad}.$$

Figure 4.12 shows the track angle distribution. The angles are given with respect to the z-axis.

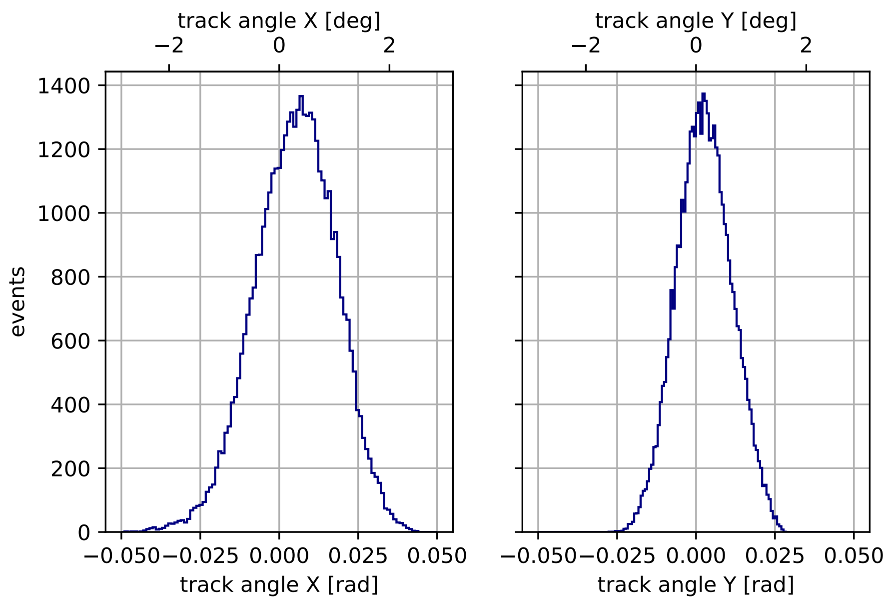

Figure 4.12: The figure depicts the track angle in x and y with respect to the z-axis. The angle distribution is narrower in y compared to x because the telescope acceptance is smaller there. This can be explained by the asymmetry of the ALPIDE sensor.

The maximum inclination angles detected in the y direction approximately match the

expected boundaries. However, the distribution of the x angle is narrower and does not reach the boundaries obtained by the telescope acceptance. This can be caused by the misalignment of the detectors, which was especially prevalent in the x direction. Software corrections up to 3.5 mm had to be made. This misalignment reduces the effective acceptance of the telescope.
However, when recalculating the acceptance, the new parameters are still not the restricting factors. This indicates that what is displayed is close to the true angle distribution in x of the incoming particles.
It can be seen that the angles are not symmetric around zero. This fact can have different reasons. On one hand, in the alignment the assumption was made that the reference planes 0 and 2 are truly positioned at the intended place. If this was not the case, the tracks can show a small systematic deviation regarding quantities such as the track angle. On the other hand, the projectile particles can be systematically inclined with respect to the z-axis of the telescope.

Chi-square distribution for different degrees of freedom

The form of the χ^2-distribution depends solely on the number of degrees of freedom (ndof or ν) in a fit. To compare the resulting chi-square distribution of the data to the theoretical expectation, it is essential to know the ndof for the fit. For the presented fit models (a straight line and a General Broken Lines trajectory), the number of degrees of freedom is determined solely by the number of measurement points if there are no additional constrains. The number of fit parameters is fixed for a given model or only dependent on the number of scattering planes, as in the GBL model. By varying the number of included planes and, consequently, the number of measurement points, the dependency of the distribution can be demonstrated.
The ndof for a straight line is calculated as follows: First the number of fit parameters has to be discussed. Generally, to describe a line in three-dimensional space following equation 3.17, two slopes and two offsets for the x and y dimensions are needed. As a result, the number of needed fit parameters to describe a straight line is four.
Next, the number of measurements is considered. On each detector a cluster is defined by a local u and v value pair or respectively a global x and y value pair. The z position is not a free parameter, because its value is determined by the plane geometry and position in space. Consequently, the sample size is two times the number of planes included in tracking.
The degrees of freedom for a straight line depending on the number of planes n_{planes} included is then given by

$$\nu_{\text{straightline}} = 2 \cdot n_{\text{planes}} - 4. \tag{4.2}$$

A General Broken Lines fit needs more parameters to define the trajectory than a simple straight line. On the other hand, it has more measurements available since the kinks constrain the fit as well. The explanation for the equation of the ndof is discussed in section 3.3.3. The dependency on the plane numbers turns out similar to the straight line case although the individual number of measurements and fit parameters are different:

$$\nu_{\mathrm{GBL}} = 2 \cdot n_{\mathrm{planes}} - 4. \tag{4.3}$$

By gradually decreasing the number of planes used for tracking, a range of different χ^2-distributions can be produced. They are shown in figure 4.13.

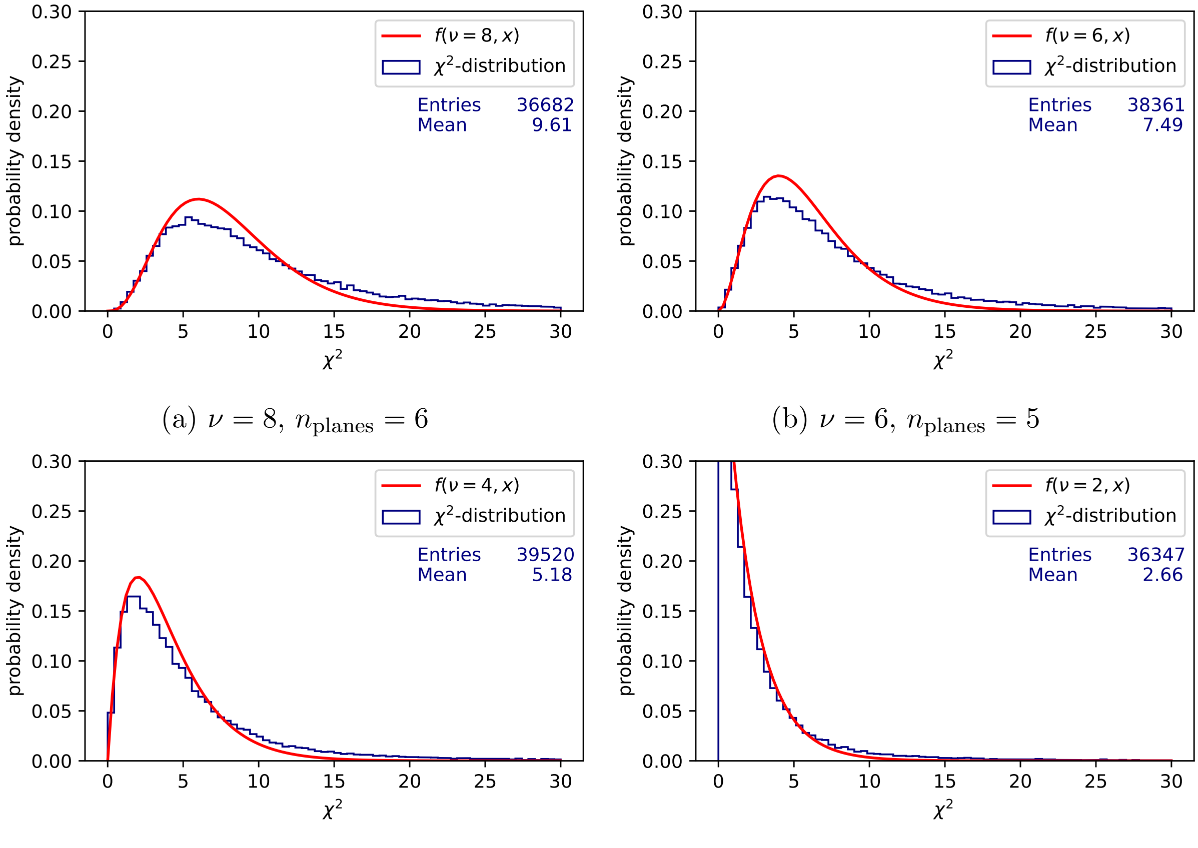

(a) $\nu = 8$, $n_{\mathrm{planes}} = 6$

(b) $\nu = 6$, $n_{\mathrm{planes}} = 5$

(c) $\nu = 4$, $n_{\mathrm{planes}} = 4$

(d) $\nu = 2$, $n_{\mathrm{planes}} = 3$

Figure 4.13: The figure depicts χ^2-distributions for a GBL fit with different degrees of freedom ν and different number of planes n_{planes} required for a track.

The distributions validate the calculation of the degrees of freedom of the fitted trajectories, because they match the theoretical distribution under variation of the degrees of freedom. It is also visible again why it was chosen to evaluate the distribution of the χ^2 and not the χ^2_{red}, which is often used when evaluating the fit quality. Due to the small number of degrees of freedom, the reduced chi-square peaks at values smaller than one. To avoid confusion with this common testing criterion (where χ^2_{red} should ideally peak at one), here it is looked for whether the normal chi-square distribution is peaking at $\max(\nu - 2, 0)$.

4.2 Comparison of different track models

Two main goals are aimed for when it comes to tracking. First, the hypothesis is to confirm that all associated measured hits belonging to a reconstructed track are generated by the same charged particle. Secondly, achieving a good tracking resolution is crucial. This is especially important for experiments where the physics analysis relies on precise trajectories for vertexing, momentum determination, and particle identification.
The main objective of the cluster size study for the ALPIDE chip is to ensure the accurate assignment of clusters to a particle. The tracking resolution will be discussed later in this chapter. Initially, the emphasis is on the implementation details of the individual track models and their ability to accurately depict the trajectory of the tracked particle. This allows for the evaluation of the tracking quality, providing information about the likelihood of correctly matching measurements to a particle.

4.2.1 Unweighted and weighted straight line fit

The appeal of an unweighted straight line fit lies in its simplicity. This fit method expects charged particles to be unaffected by external forces and thus travel through the telescope in a straight path. To construct the χ^2-sum in this case, only the measurements and their covariance matrices need to be provided.
In the introductory section 3.3.1, a simplified setup was depicted where the global z direction is always perpendicular to the detector planes. However, in the studied data, the detector planes were rotated. This introduces a non-linear dependence of the fit parameters in the chi-square function when the residuals are constructed in the local detector system (u, v, w) [24]. With iterative methods, such a non-linear chi-square can be minimised. It is, nevertheless, very computationally expensive.
The iterative calculation can be avoided by constructing the residual to the fitted trajectory in the global system (x, y, z)[2]. The linear function describing the straight line is therefore evaluated at the z coordinate of the measurement point on each plane. Consequently, the local covariance matrices on the detector planes need to be transformed into the global system.
The ALPIDE chip is locally assigned with an intrinsic resolution in u and v. An uncer-

[2]The local residuals can then be approximated with their projections on the respective axis.

tainty in w is not defined. This originates from the fact that the detector is primarily used perpendicular to the projectile particle. Here, the z position is of lesser importance for the tracking resolution, and thus no uncertainty needs to be taken into account.
A fallacy occurs when the detector is rotated around x or y and the resolution is not reconsidered. For instance, if the plane is rotated by $90\,^\circ$ around the y axis the spatial resolution in x should be zero, because the projection of the local uncertainty in the global x space vanishes. However, this can not be true. In fact, the spatial resolution in x and y worsens with a rotation of the detector plane [15]. Apart from simple geometry reasons (such as the actual uncertainty of the ALPIDE in the w direction), this dependence is also influenced by internal charge collection processes and the cluster size, which increases with a stronger inclination.
For simplicity in this study, it is assumed that the global spatial resolution is 5 µm, which is the intrinsic resolution associated with an ALPIDE. The assumption hereby is that the intrinsic resolution does not increase, and the inclination of the detector planes are small enough to be neglected. This was found to be a good approximation for rotations less then about $30\,^\circ$. The fitted data produce a χ^2-distribution, as shown in figure 4.14.

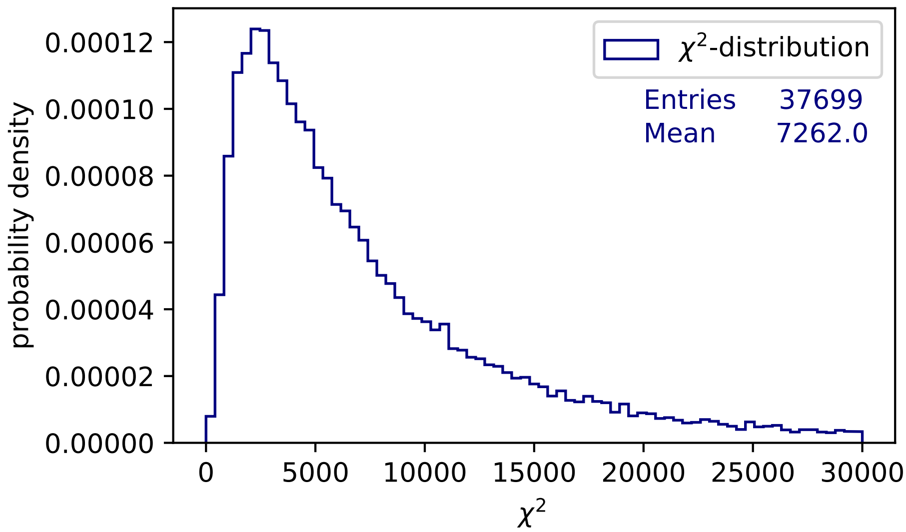

Figure 4.14: The figure depicts the χ^2-distribution for unweighted straight line fits of particles strongly affected by multiple scattering. The distribution shows that the model does not represent the actual behaviour of the particles. The mean is expected to be the number of degrees of freedom, which is eight. However, the distribution exhibits a mean with a value substantially higher.

The measurement uncertainties are determined only by the detector resolution and do not account for uncertainties arising from multiple scattering. Consequently, for low momentum particles, the uncertainties are significantly underestimated, leading to very high χ^2-values.

To account for the uncertainties introduced by multiple scattering more accurately, a weighted straight line fit can be employed. The covariance matrix incorporates both the detector resolution and the uncertainties arising from multiple scattering. Again, the residuals and the covariance matrices are constructed in the global system. It is approximated that all particles propagate almost parallel to the z axis.

By employing this fitting method, a more reliable estimation of the uncertainties is achieved. Consequently, smaller uncertainties are assigned to measurements closer to the beginning of the telescope (starting from the detector resolution on the first plane), while larger uncertainties are assigned to measurements at planes further back in the telescope. The chi-square distribution resulting from this weighted straight line fit is depicted in figure 4.15.

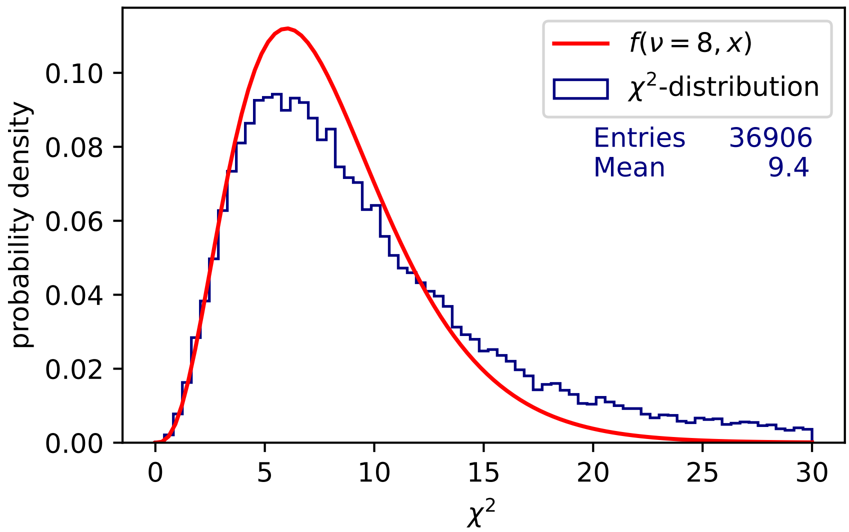

Figure 4.15: χ^2-distribution for weighted straight line fits of particles affected by multiple scattering. The peak is at the correct position but the distribution shows a systematic asymmetry.

The χ^2-values are small and show a sensible peak. A prominent asymmetry, however, raises questions. Apparently, there are to many entries at high chi-square values. To resolve the cause, a look at the residual distribution is helpful. An exemplary residual distribution of plane 2 is portrayed in figure 4.16a. It shows the Gaussian fit of the inner part of the distribution. The data reveal that the residuals do not follow a simple Gaussian distribution. The inner part is described well by a single Gaussian, but the whole distribution exhibits tails towards both lower and higher values.

A single Gaussian distribution is primarily expected due to the detector resolution and the position displacement from multiple scattering, both of which are expected to follow a Gaussian distribution. Their combination into one uncertainty corresponds to a multi-

plication of two Gaussian probability density functions which in turn is a Gaussian.
In fact, the angle or displacement from multiple scattering is not entirely Gaussian. Only the inner part (98 %) can be described as a Gaussian distribution. On the other hand, the model expects Gaussian distributed variables. This serves the simplicity of the model and enables the usage of the chi-square formalism. Therefore, the tails of the residuals are not treated correctly, generating in turn to many high χ^2-values.
A better description for the distribution of the residuals is a double Gaussian probability density function [18]. It is presented in figure 4.16b. The core and tails are modelled by two Gaussian functions, where the the standard deviation of the core is smaller than the standard deviation of the Gaussian function which models the tails.

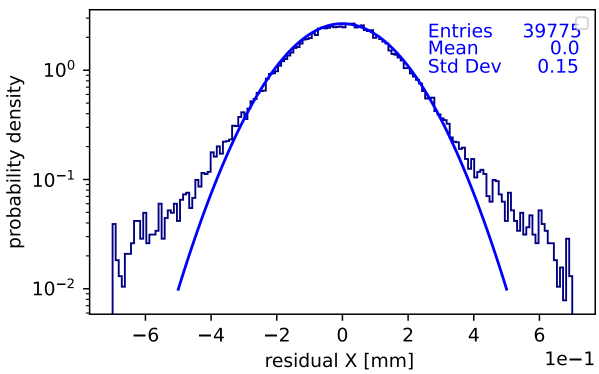

(a)

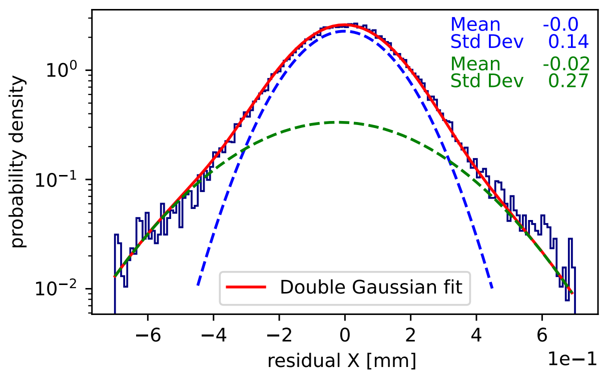

(b)

Figure 4.16: The figure shows the residual of plane 2 resulting from a weighted straight line fit. (a) depicts a fit with a single Gaussian function. In (b) a double Gaussian was fitted that originates from the convolution of two single Gaussian functions depicted in blue and green.

Nonetheless, for the purpose of this thesis the model of a weighted straight line is adaptable to describe particles affected by multiple scattering. It enables a mostly clear reconstruction of true particle trajectories and allows a detection of uncorrelated hit points. With a cut on the residuals distribution or respectively the χ^2-value, events that have a high probability to be solely produces by a projectile particle from the beam can be filter.
However, the increasing measurement uncertainty towards the last planes of the telescope is introducing more room for falsely including uncorrelated hit points. Additionally, the full performance concerning the spatial resolution of the detector can not be used. This motivates the use of a fit model that does not correlate the scatterers within the telescope and thus achieves a better spatial resolution overall.

4.2.2 General Broken Lines fit

The broken lines method is based on refitting an initial trajectory while including the description of multiple scattering. The initial trajectory was selected as a weighted straight line. This choice is feasible due to the fact that, in test beam conditions, the speed of the fit generally has only a small significance. In cases where speed becomes crucial and the number of scattering points is substantial, it is advisable to explore an internal seeding procedure tailored to meet the requirements. One of such a method was presented in chapter 3.2.2.
In situations where some quantities of the initial projectile particle are partially known, these can serve as an external seed. If, for example, it is known that the initial particle must have propagated parallel to the z-axis, as is often the case with high-quality or high momentum particle beams, this information can be employed in conjunction with the first hit position to construct an initial trajectory.
As the protons in this study traversed a significant amount of material before being detected in the telescope, their propagation does not align parallel to the z-axis as it can be seen in figure 4.12. Consequently, no external information could be utilised in this case.

The implementation of the GBL software begins by constructing the Jacobian $\mathbf{T}_\mathrm{i}$ from equation 3.36. It characterises the transition under variation of the curvilinear track parameters of the weighted straight line from one track point i to the next i + 1. For a track point at the path length s_i, the transformation of the parameters to the same set of parameters at the track point at arc-length $s_\mathrm{i+1}$ is precisely described in [39]. The crucial entries in the Jacobian matrix are as follows, while the remaining entries are either zero or become zero when there is no magnetic field present.

$$\frac{\partial(q/p_\mathrm{i+1})}{\partial(q/p_\mathrm{i})} = \frac{\partial\lambda_\mathrm{i+1}}{\partial\lambda_\mathrm{i}} = \frac{\partial\phi_\mathrm{i+1}}{\partial\phi_\mathrm{i}} = \frac{\partial x_{\perp,\mathrm{i+1}}}{\partial x_{\perp,\mathrm{i}}} = \frac{\partial y_{\perp,\mathrm{i+1}}}{\partial y_{\perp,\mathrm{i}}} = 1 \tag{4.4}$$

$$\frac{\partial x_{\perp,\mathrm{i+1}}}{\partial\phi_\mathrm{i}} = \cos\lambda_\mathrm{i} \cdot (s_\mathrm{i+1} - s_\mathrm{i}) \tag{4.5}$$

$$\frac{\partial y_{\perp,\mathrm{i+1}}}{\partial\lambda_\mathrm{i}} = s_\mathrm{i+1} - s_\mathrm{i} \tag{4.6}$$

In words, for a straight line, the variation of a track parameter directly translates to the same track parameter at the next point. This is indicated by equation 4.4. Hereby, the momentum is expected to remain constant throughout the entire telescope. Additionally, a variation of the momentum direction, which is a modification of λ or ϕ (the angles describing the tangent of the track at the intersection point on the plane), induces a change of the offset parameters at the next track point indicated with equations 4.5 and

4.6. The whole matrix reads as follows:

$$T_{\mathrm{i}} = \frac{\partial(q/p, \lambda, \phi, x_\perp, y_\perp)_{\mathrm{i+1}}}{\partial(q/p, \lambda, \phi, x_\perp, y_\perp)_{\mathrm{i}}} = \begin{pmatrix} 1 & 0 & 0 & 0 & 0 \\ 0 & 1 & 0 & 0 & 0 \\ 0 & 0 & 1 & 0 & 0 \\ 0 & 0 & \cos\lambda_{\mathrm{i}} \cdot (s_{\mathrm{i+1}} - s_{\mathrm{i}}) & 1 & 0 \\ 0 & (s_{\mathrm{i+1}} - s_{\mathrm{i}}) & 0 & 0 & 1 \end{pmatrix}. \tag{4.7}$$

The residual to the initial trajectory is constructed in the curvilinear system since the track points are also defined in the curvilinear system. To derive the quantity coming from the local residuals in the detector plane, the projection $\mathbf{P} = \frac{\partial(x_\perp, y_\perp)}{\partial(u,v)}$ is used. It projects the detector residuals into the curvilinear frame. The components are

$$\mathbf{P} = \begin{pmatrix} \mathbf{e}_{x_\perp}\mathbf{e}_u & \mathbf{e}_{x_\perp}\mathbf{e}_v \\ \mathbf{e}_{y_\perp}\mathbf{e}_u & \mathbf{e}_{y_\perp}\mathbf{e}_v \end{pmatrix}, \tag{4.8}$$

where $\mathbf{e}$ is the base vector of the respective system. The covariance matrix stating the local detector resolution has to be projected into the curvilinear system as well in order to align with the residuals. The covariance of the kink residuals has to be declared in the detector system according to equation 3.30. This concludes the details on the implementation and paves the way to delve into the results of this model.

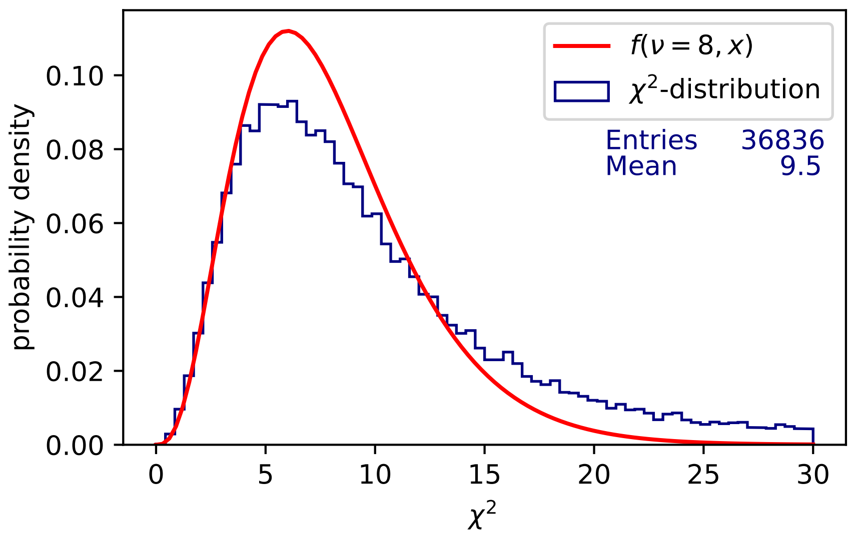

Figure 4.17: The figure shows a χ^2-distribution where a General Broken Lines fit was employed. The distribution shows that the GBL model satisfies the need for a method that reconstructs particles affected by multiple scattering. For low chi-square values the the outcome exactly matches the expectation. For higher values a small asymmetry is visible, explainable by the tails in the multiple scattering distribution.

The resulting χ^2-distribution is depicted in figure 4.17. The agreement with the expected distribution is good, taking into account the previous explanation of the double Gaussian probability density function of the multiple scattering angle. In the broken lines model, the assumption regarding the scattering angle distribution is identical to that of the weighted straight line. The uncertainty for the kink residuals is assumed to follow a Gaussian distribution. This does not precisely align with the reality but is a good approximation.
What distinguishes the GBL method from the weighted straight line method is the associated measurement resolution. For the GBL approach this measurement resolution is solely dependent on the spatial detector resolution. Conversely, for a weighted straight line fit the measurement uncertainty is dependent on the scattering angles of all scatterers in front of the examined detector. Consequently, the uncertainty increases plane by plane and only the first detector keeps its initial spatial resolution.
A smaller measurement resolution, and consequently a smaller tracking resolution, allows for better differentiation of closely located uncorrelated hit points from the trajectory. In other words, even if a hit point is closer to the examined trajectory but not caused by the projectile proton, it can still be accurately identified as uncorrelated. As a result, the broken lines approach enhances the ability to identify outliers, which refer to measurements that are either not correlated or only indirectly correlated with the projectile particle.
Overall, a broken line closely approximates the true trajectory followed by a low-momentum particle. The fact that the measurement uncertainties are uncorrelated and equal to the true detector resolution while the method models the charged particle realistically results in a good tracking resolution. The details regarding the tracking resolution will be covered in the subsequent section.
There are also track models that implement non-Gaussian uncertainties for instance the Gaussian-Sum Filter [17]. The Gaussian-Sum Filter allows the probability density functions to be mixtures of normal pdfs or Gaussian sums. It is equivalent to parallel Kalman filters, where the total chi-square is calculated with a weighted sum of the single (parallel) χ^2-sums.
However, this flexibility comes at the cost of losing the ability to calculate the chi-square probability density function analytically. Furthermore, the computational time required for the Gaussian-Sum Filter is significantly higher compared to models like the Kalman filter or GBL. As a result, it is primarily employed for particles that exhibit pronounced changes in direction within their trajectories, thus the single Gaussian approximation of uncertainties is not representative. Electrons are a prime example of such particles.

4.3 Tracking Resolution

An accurate tracking resolution is essential for particle physics experiments, particularly for tasks such as vertexing and momentum determination. The tracking resolution refers to the precision with which the reconstructed trajectory can be determined at any given position z. This resolution is calculated by propagating the uncertainties associated with the fit parameters.

The covariance matrix of the fit parameters is dependent on the multiple scattering angles, the intrinsic detector resolutions and the plane positions. In general, a larger distance between planes leads to an improvement in resolution. Conversely, a larger lever arm, which refers to the distance travelled by the particle in between two detectors increases the multiple scattering in the air and additionally worsens the ability to reject outliers. As multiple scattering effects become more significant, the overall tracking resolution at the detection planes approaches the intrinsic resolution of the detector.

The track points and their resolution at the detector planes are particularly intriguing. When the initial trajectories of the particles are assumed to be approximately parallel to the z-axis of the telescope, a uniform detector resolution can be assigned to the experimental setup. This resolution is evident in the residual distribution observed at the detector plane.

The residuals, which represent the difference between the measured values and the expected values based on the fitted trajectory, exhibit distinct probability density functions depending on whether the measurement on the plane was used for tracking or not. Biased and unbiased residuals are commonly distinguished in this context.

4.3.1 Biased and unbiased residuals

To summarise once again, the residuals r_i on a plane i represent the distance between the track point x_i and the corresponding measurement point m_i and are given by

$$r_\mathrm{i} = x_\mathrm{i} - m_\mathrm{i}.$$

When the measurement on plane i is not included in the track fit, the uncertainties of x_i and m_i are independent. In this case, the residual is called unbiased. Consequently, the squared standard deviation of the unbiased residual, incorporating error propagation, is

$$\sigma^2_{\text{unbiased residual,i}} = \left(\sigma_{x,\mathrm{i}} \cdot \frac{\partial r_\mathrm{i}}{\partial x_\mathrm{i}}\right)^2 + \left(\sigma_{m,\mathrm{i}} \cdot \frac{\partial r_\mathrm{i}}{\partial m_\mathrm{i}}\right)^2 = \sigma^2_{x,\mathrm{i}} + \sigma^2_{m,\mathrm{i}}, \tag{4.9}$$

where $\sigma_{x,\mathrm{i}}$ represents the tracking resolution at plane i, and $\sigma_{m,\mathrm{i}}$ denotes the resolution of the measurement.

However, if the measurement on plane i is included in the track fit, the track position becomes dependent on it. Therefore, the derivative $\frac{\partial r_\mathrm{i}}{\partial m_\mathrm{i}}$ also includes a component of $\frac{\partial x_\mathrm{i}}{\partial m_\mathrm{i}}$. As a result, the standard deviation of a biased residual calculates as:

$$\sigma^2_{\text{biased residual,i}} = \sigma^2_{m,\mathrm{i}} - \sigma^2_{x,\mathrm{i}}. \tag{4.10}$$

A more detailed calculation can be found in [45]. The same principle accounts for the residuals of the kink angles, where the track point is the kink angle and the measurement is the expected value of the kink, hence zero. The uncertainty of the kink angles arises from the propagation of the fit parameters and the uncertainty for the expected value of the kink angles is the standard deviation following the Highland formula given in equation 2.3.

4.3.2 Pulls

Pulls are calculated by normalising the residuals with the standard deviation of the expected distribution. Ideally, the resulting distribution should follow a standard normal distribution, characterised by a mean of zero and a standard deviation of one. For biased residuals, the biased pull is obtained by dividing the biased residual by the expected standard deviation derived from equation 4.9. Mathematically, it can be expressed as follows

$$p_{\text{biased,i}} = \frac{r_{\text{biased,i}}}{\sqrt{\sigma^2_{m,\mathrm{i}} - \sigma^2_{x,\mathrm{i}}}}. \tag{4.11}$$

Pulls provide a valuable tool for verifying the accuracy of the fits. In essence, checking the pulls of the measurement residuals and the residuals of the kink angle is akin to examining the chi-square distribution. It is particularly useful when investigating specific issues that may arise during the fitting procedure.

On the contrary, the pulls or residuals themselves serve as the focal point for sensor characterisation. When evaluating an unfamiliar sensor, the inherent resolution can be determined by analysing these pull distributions. Ideally, a configuration should be established wherein a collection of well-known detectors is arranged for tracking purposes, with the device under test (DUT) positioned in the centre of the sensor array. The middle location is chosen as it typically offers the highest tracking resolution, having detection planes on both sides. By excluding the DUT from the tracking process, unbiased residuals can be observed, providing valuable insights into the intrinsic detector resolution.

Alternatively, it is also possible to examine the detector resolution using biased residuals, but this approach involves an iterative process and is not the preferred method. The procedure involves testing multiple intrinsic resolutions, performing fits, and constructing biased pulls for each resolution. By analysing the resulting pull distributions, the correct spatial detector resolution can be identified when it exhibits the desired characteristics of a standard normal distribution. However, due to the iterative nature of this approach, it is generally less favoured compared to the other method.

Returning to the data currently under investigation, the aforementioned method provides an opportunity to validate the assumption made in section 4.2.1. In that section, it was assumed that at a rotation angle of 30° and for protons with a momentum of 470 MeV/c, the detector resolution projected into the global space is approximately 5 µm. This corresponds to a local resolution of around $\sigma_m \approx 6$ µm.

figure 4.18 presents the pull distribution of the GBL fit for plane 1 as an example. Various spatial resolutions were tested to observe their impact on the pull distribution. The analysis confirmed that a local spatial resolution of approximately 6 µm in both u and v dimensions yields the best agreement with the data, i.e., a pull distribution whose standard deviation is closest to one.

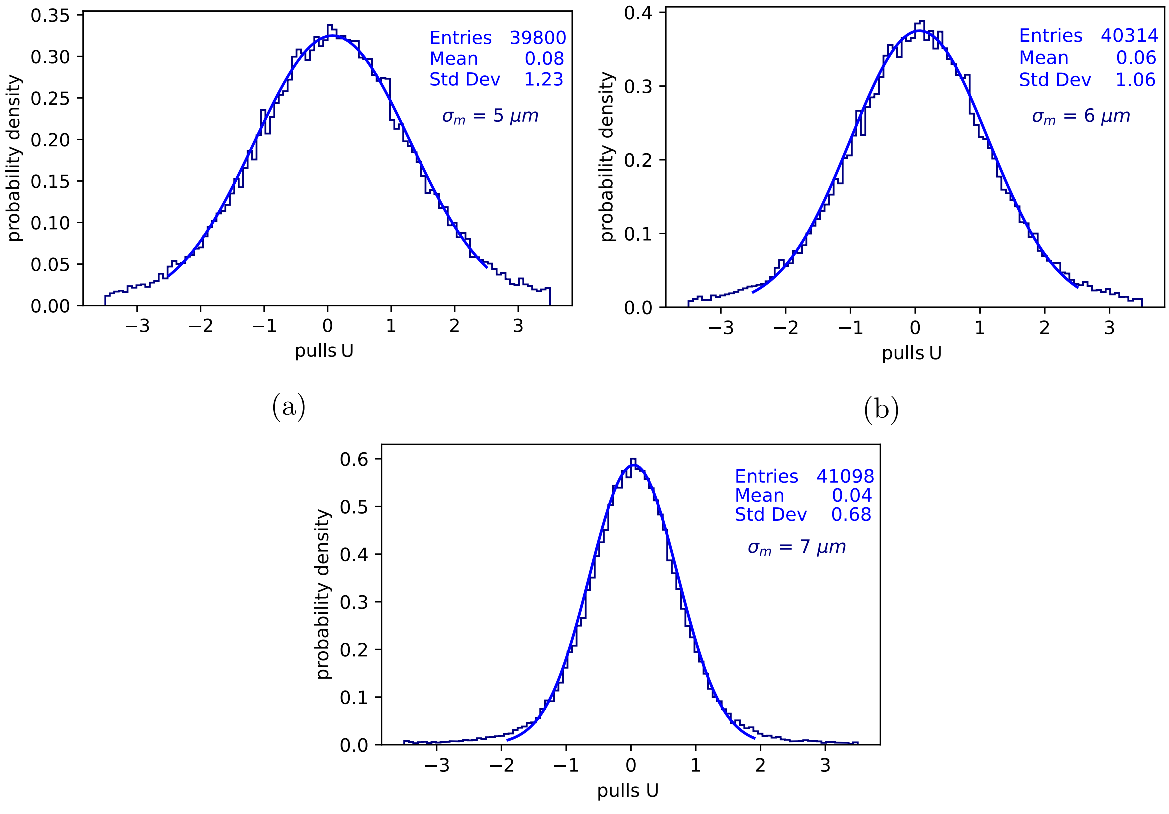

Figure 4.18: The figure illustrates the pull distribution in u (local detector system) on plane 1 for a GBL fit. Three different initial detector resolutions were considered: (a) $\sigma_m = 5$ µm, (b) $\sigma_m = 6$ µm, and (c) $\sigma_m = 7$ µm. Among these options, the best result, which closely resembles a standard normal distribution, was achieved with an intrinsic resolution of $\sigma_m = 6$ µm.

The typical spatial resolution associated with an ALPIDE chip is 5 µm in the local detector system. This value is derived from testbeam measurements with no rotation of the planes and minimum ionising projectile particles. An average cluster size of $2.5 - 3$ gives the best resolution, which is around 5 µm [30]. In the current study, the average cluster size is significantly larger, around 5.1, due to the rotation of the planes and the presence of low-momentum protons, which experience a greater energy loss in the rising part of the Bethe-Bloch formula. Consequently, a larger intrinsic resolution is expected. The small increase in the resolution in this case is not significant for the overall reconstruction of the particle. Nevertheless it should not be neglected and especially for planes rotated at larger angles it might have a greater importance.
Simultaneously, particles that experience greater energy loss tend to generate larger clusters, thereby degrading the spatial resolution. This phenomenon remains consistent when the threshold is maintained at the same settings as for minimum ionising particles. Consequently, a question arises: Can the resolution for low momentum particles be enhanced by increasing the threshold value, thus reducing the average cluster size? This approach could be especially beneficial for setups focused on measuring particles with high energy loss exclusively.

With this, the reconstruction of particles is complete. The whole scope from raw hit clusters to precisely reconstructed particles was discussed. In the beginning an accurate energy loss calculation of the projectile particles was performed to understand the extent of scattering experienced by the protons in the telescope. Then, the alignment was presented, which is a crucial step in the analysis. It had to be guaranteed that even under difficult conditions, namely strong scattering in the telescope as well as inclined tracks, the software alignment yields precise and predictable results.
The next step was to introduce the filters that were used to select specific events. Here the goal was to only keep the data that were produced by beam protons and reject uncorrelated clusters. In addition to applying coarser cuts, a more refined selection can be achieved by tracking the particles and evaluating the χ^2-value of their fits. Three different tracking models were discussed of which, the weighted straight line and the General Broken Lines method were able to accurately represent the passage of low momentum protons. Especially the broken line fit has revealed that, with its good tracking resolution and the independent consideration of the multiple scattering contribution, it is able to reject outliers to a high degree of efficiency.
Lastly, the tracking resolution, the pulls and the difference between biased and unbiased residuals were discussed. This has shown that the interpretation of the residual and pull distributions is an important step for the validation of the reconstruction procedure.

Chapter 5

Summary, conclusion and outlook

Summary

In an effort to enhance the impact parameter resolution and tracking efficiency, especially for particles with low transverse momenta, the ALICE detector underwent an upgrade that included the transition to a purely digital tracking system featuring ALPIDE sensors. Nevertheless, this update resulted in the loss of the ability to determine the specific energy loss of particles. To address this limitation and explore potential particle identification improvements, a study was conducted to investigate a possible link between the energy loss and the cluster size in the ALPIDE chips. One step towards this goal consisted in recording data with low energy protons during a dedicated testbeam campaign.
Low-energy protons experience significant multiple scattering as they traverse a testbeam telescope setup. Consequently, reconstructing their trajectory becomes a challenging task. A simple straight line trajectory is inadequate to represent their path, necessitating the use of specific tracking models capable of accommodating directional changes within the trajectory. To address this issue, the General Broken Lines track model was introduced. This model is designed to account for changes in the trajectory with the use of kink angles, providing a more accurate representation of the path of a proton as it encounters matter. The specific implementation details of this model were thoroughly explained, contributing to a better understanding of the variables utilised by the model.
To perform the software alignment of the telescope, a two-step process was employed. Initially, a simplified straight-line fit was used for the track-based alignment. In the second step, full precision was achieved by employing the General Broken Lines fit. The chi-square formalism played a crucial role in determining the best fit parameters and assessing the track quality. During this process, it was essential to filter out uncorrelated clusters that were not produced by the initial projectile particles. This filtering step was necessary to avoid possible bias in the cluster size analysis. As the fit model more accurately approximates the true path of the particle being tracked, its ability to reject

outliers improves.
The General Broken Lines formalism demonstrated its capability to accurately capture the characteristics of beam protons affected by multiple scattering in the telescope. A Gaussian approximation of the scattering angle proved to be sufficiently good, facilitating a successful and unambiguous trajectory reconstruction. Consequently, clusters on the ALPIDE could be confidently attributed to the intended projectile particles with a high probability.
Furthermore, this study provided valuable insights into the spatial resolution of an ALPIDE. Biased and unbiased residuals from tracking were thoroughly discussed, allowing for the evaluation of resolution changes under different experimental conditions. Specifically, the combination of an inclination of the sensor plane and an increased energy deposit of the incident particle led to an increase in the intrinsic resolution.

Conclusion

This study introduced a diverse range of track models, including both established ones, widely used in various experiments, and newer variations aimed at enhancing the track reconstruction of low momentum particles, particularly those that are affected by multiple scattering. The significance of tracking low momentum particles has been demonstrated to be crucial not only for large-scale experiments, but also for small-scale ones. Consequently, the development of reliable methods for tracking such particles becomes increasingly important.
In ALICE, extending the lower momenta range is driven by the rich physics that can be explored, significantly impacting the overall modelling of the quark-gluon plasma. However, the importance of this extension goes beyond high-energy physics. In the field of medical physics, as the utilisation of low momentum ions in cancer treatment continues to expand, there is a growing need for applications that involve tracking heavy, low momentum particles.
Ensuring a proper understanding of every variable and facilitating accurate analysis becomes paramount when applying a tracking model. Due to the utilisation of numerous coordinate systems and the potential bias in examined variables, it becomes crucial to be aware of these aspects and interpret them correctly. This is particularly critical in testbeam experiments involving low momentum particles, as the procedure from raw hit clusters to reconstructed tracks can be highly sensitive. The alignment procedure, in particular, is profoundly influenced by divergent beams and scattered particles, necessitating the exploration of novel approaches to achieve a successful alignment. Addressing these challenges is essential to obtain reliable and meaningful results from the experimental data.

By employing a tracking model that aligns with the underlying physics governing the projectile particle, it becomes feasible to achieve a reconstruction with high tracking resolution. The ability to reject outliers, up to a certain extent determined by the multiple scattering angle, further enhances the accuracy of the reconstruction. However, this process heavily relies on the accurate estimation of all variables within the experimental setup. Hence, to ensure precise results, extensive knowledge about the tracking detector becomes indispensable, particularly in untested or challenging conditions. This includes a thorough understanding of the characteristics, response, and limitations of a detector. By leveraging this wide-ranging knowledge of the tracking detector, researchers can confidently optimise the tracking model and make informed decisions in handling potential outliers and uncertainties. Moreover, it enables them to adapt the model to varying experimental conditions, facilitating reliable and robust tracking performance.

Outlook

Multiple scattering poses a significant challenge for physicists aiming to accurately track particles. While tracking models such as the Kalman filter and General Broken Lines can reconstruct scattered particles with reasonable precision, they rely on the assumption of Gaussian uncertainties. However, especially the study of electrons that undergo Bremsstrahlung has highlighted the need for track models that can handle non-Gaussian uncertainties [8]. Unfortunately, these models often prove unsuitable for high-rate experiments or analyses with limited computational resources due to their substantial computation time. Hence, the discussion of track fitting quality extends beyond mere accuracy; it also involves evaluating the speed of the algorithm.

With the traditional approaches to boosting CPU performance reaching a plateau, the focus shifts to algorithms that can be parallelised for improved efficiency [40]. Here, a new three-dimensional track fit with multiple scattering can be mentioned that works with a sum of independent fits of hit triplets [10]. This enables an easy parallelisation in addition to its inherent fast processing capabilities.

Returning to the setup of the current study, a successful method has been demonstrated for aligning and tracking low momentum protons at the testbeam. The next challenge is to apply this procedure to data from the same study, where the conditions are even more demanding – involving stronger inclinations of the detectors and lower proton energies. In such cases, the total number of events is reduced, making it more important to reconstruct every particle that was recorded.

The data taken with 120 MeV protons and a 30° plane rotation were sorted to include only events where there is only one cluster found on each plane. This reduces the available tracks significantly. It is more sensible to also include events with multiple clusters on a

detector and use the chi-square value of the fits to find the correct trajectory.
When the setup is still unaligned, it is not possible to distinguish correlated and uncorrelated hits. However, with iterative alignments, the outliers are revealed step by step. This is because the alignment enhances the quality of a true track. In other words this means that the chi-square value gets smaller as the position of the detectors gets closer to the true detector position. A track including an uncorrelated hit on the other hand does not improve in the aligning procedure and therefore can be identified. As the active area of the detector reduces in size due to rotation, there is an increased likelihood of events where particles do not hit every plane of the detector. Rather than rejecting these events, considering them could present another valuable opportunity to expand the statistics.
Another challenge arises under these conditions: Sensors are typically characterised under "normal conditions" with perpendicular incidence of relativistic particles on the detectors. However, it is important to recognise that sensor parameters can vary under different conditions. Notably, studies have demonstrated that the tracking resolution is influenced by the rotation of the sensor [15] and may also differ for different types and energies of particles. Therefore, for precise reconstruction, an individual characterisation of sensors under specific conditions would be highly advantageous. In this context, simulation studies play a crucial role. When the charge collection process is accurately simulated, it allows for estimating the spatial resolution in advance.
Finally, it offers the possibility to identifying regions where sensors perform optimally. This knowledge can inform decisions such as sensor rotation or adjusting threshold settings to enhance the spatial resolution when planing specific experimental setups.

Acknowledgements

I am deeply happy and profoundly grateful to Prof. Dr. Silvia Masciocchi for providing me with the incredible opportunity to join her exceptional research team, where special expertise converges with kind-hearted and supportive individuals. The experiences I gained have immensely enriched my skills and contributed to my personal growth. I am especially thankful for the understanding, respectful, knowledgeable, and motivating environment that Silvia has created.

I extend my sincere thanks to Dr. Kai Schweda for accepting the role of my second examiner.

My heartfelt appreciation goes to Bogdan Bildaru, whose exceptional humour and knowledge were invaluable in guiding me throughout this journey. His support has been truly irreplaceable and deserving of the warmest gratitude.

As I reflect on everything, my thoughts are drawn back to my beloved partner and my loving parents. Their unwavering and unconditional support has been a constant source of joy, happiness, and stability in my life, for which I am endlessly thankful.

References

[1] W Adam et al. “Stand-alone cosmic muon reconstruction before installation of the CMS silicon strip tracker”. In: *Journal of Instrumentation* 4 (Jan. 2009), P05004.

[2] Gianluca Aglieri Rinella. “The ALPIDE pixel sensor chip for the upgrade of the ALICE Inner Tracking System”. In: *Nuclear Instruments and Methods in Physics Research Section A: Accelerators, Spectrometers, Detectors and Associated Equipment* 845 (2017). Proceedings of the Vienna Conference on Instrumentation 2016, pp. 583–587. ISSN: 0168-9002. DOI: `https://doi.org/10.1016/j.nima.2016.05.016`. URL: `https://www.sciencedirect.com/science/article/pii/S0168900216303825`.

[3] Petteri Aimonen. *Basic concept of Kalman filtering*. Available at `https://en.wikipedia.org/wiki/File:Basic_concept_of_Kalman_filtering.svg` (2023/07/16).

[4] B Abelev et al and (The ALICE Collaboration). “Technical Design Report for the Upgrade of the ALICE Inner Tracking System”. In: *Journal of Physics G: Nuclear and Particle Physics* 41.8 (July 2014), p. 087002. DOI: `10.1088/0954-3899/41/8/087002`. URL: `https://dx.doi.org/10.1088/0954-3899/41/8/087002`.

[5] B Abelev et al and (The ALICE Collaboration). “Upgrade of the ALICE Experiment: Letter Of Intent”. In: *Journal of Physics G: Nuclear and Particle Physics* 41.8 (July 2014), p. 087001. DOI: `10.1088/0954-3899/41/8/087001`. URL: `https://dx.doi.org/10.1088/0954-3899/41/8/087001`.

[6] ALICE Collaboration. *A Large Ion Collider Experiment*. Available at `https://alice.cern/` (2023/07/17).

[7] Luca Amendola. *Statistical Methods*. Lecture Notes. Heidelberg University, summer term 2022.

[8] T. Atkinson. “Reconstruction of electrons with the Gaussian-Sum filter in the ATLAS inner detector”. In: *IEEE Nuclear Science Symposium Conference Record, 2005*. Vol. 1. 2005, pp. 148–152. DOI: `10.1109/NSSMIC.2005.1596226`.

[9] Yu Belikov, K Safarík, and B Batyunya. *Kalman Filtering Application for Track Recognition and Reconstruction in ALICE Tracking System*. Tech. rep. Geneva: CERN, 1997. URL: `https://cds.cern.ch/record/689414`.

[10] Niklaus Berger et al. "A new three-dimensional track fit with multiple scattering". In: *Nuclear Instruments and Methods in Physics Research Section A: Accelerators, Spectrometers, Detectors and Associated Equipment* 844 (2017), pp. 135–140. ISSN: 0168-9002. DOI: `https://doi.org/10.1016/j.nima.2016.11.012`. URL: `https://www.sciencedirect.com/science/article/pii/S016890021631138X`.

[11] Matthias Bartelmann Björn M. Schäfer. *Statistics: The Logic of Science*. Heidelberg University.

[12] V. Blobel. "Software alignment for tracking detectors". In: *Nuclear Instruments & Methods in Physics Research Section A-accelerators Spectrometers Detectors and Associated Equipment* 566 (2006), pp. 5–13.

[13] ALICE collaboration. "Alignment of the ALICE Inner Tracking System with cosmic-ray tracks". In: *Journal of Instrumentation* 5.03 (Mar. 2010), P03003–P03003. DOI: `10.1088/1748-0221/5/03/p03003`. URL: `https://doi.org/10.1088%2F1748-0221%2F5%2F03%2Fp03003`.

[14] Z. Drasal and W. Riegler. "An extension of the Gluckstern formulae for multiple scattering: Analytic expressions for track parameter resolution using optimum weights". In: *Nuclear Instruments and Methods in Physics Research Section A: Accelerators, Spectrometers, Detectors and Associated Equipment* 910 (Dec. 2018), pp. 127–132. DOI: `10.1016/j.nima.2018.08.078`. URL: `https://doi.org/10.1016%2Fj.nima.2018.08.078`.

[15] Natalia Emriskova. "Analysis of test beam data of ALPIDE, the final Monolithic Active Pixel Sensor (MAPS) prototype for the ALICE ITS upgrade ". In: (2017). URL: `https://cds.cern.ch/record/2293610`.

[16] R. Fruhwirth. "Application of Kalman filtering to track and vertex fitting". In: *Nucl. Instrum. Meth. A* 262 (1987), pp. 444–450. DOI: `10.1016/0168-9002(87)90887-4`.

[17] R Frühwirth. "Track fitting with non-Gaussian noise". In: *Computer Physics Communications* 100.1 (1997), pp. 1–16. ISSN: 0010-4655. DOI: `https://doi.org/10.1016/S0010-4655(96)00155-5`. URL: `https://www.sciencedirect.com/science/article/pii/S0010465596001555`.

[18] R. Frühwirth and M. Regler. “On the quantitative modelling of core and tails of multiple scattering by Gaussian mixtures”. In: *Nuclear Instruments and Methods in Physics Research Section A: Accelerators, Spectrometers, Detectors and Associated Equipment* 456.3 (2001), pp. 369–389. ISSN: 0168-9002. DOI: https://doi.org/10.1016/S0168-9002(00)00589-1. URL: https://www.sciencedirect.com/science/article/pii/S0168900200005891.

[19] Rudolf Frühwirth and Are Strandlie. “Track Models”. In: *Pattern Recognition, Tracking and Vertex Reconstruction in Particle Detectors*. Cham: Springer International Publishing, 2021, pp. 49–80. ISBN: 978-3-030-65771-0. DOI: 10.1007/978-3-030-65771-0_4. URL: https://doi.org/10.1007/978-3-030-65771-0_4.

[20] Norbert Köckler Hans Rudolf Schwarz. *Numerische Mathematik*. 7th ed. Vieweg+Teubner Verlag Wiesbaden, 2009.

[21] U. Hartenstein. “Dissertation ”Track based alignment for the MU3E pixel detector””. In: (2019).

[22] Johannes Hensler. “Bachelor thesis ”Simulation of reaction cross-section measurement for protons in aluminium in the energy range of 48-232 MeV using Geant4””. In: (2023).

[23] Lennart Huth. *A high rate testbeam data acquisition system and characterization of high voltage monolithic active pixel sensors*. eng. Heidelberg, 2019, 1 Online–Ressource (xvi, 201 Seiten). DOI: 10.11588/heidok.00025785. URL: http://nbn-resolving.de/urn:nbn:de:bsz:16-heidok-257853.

[24] Veikko Karimäki. *Straight Line Fit for Pixel and Strip Detectors with Arbitrary Plane Orientations*. Tech. rep. Geneva: CERN, 1999. URL: https://cds.cern.ch/record/687146.

[25] Claus Kleinwort. “General broken lines as advanced track fitting method”. In: *Nuclear Instruments and Methods in Physics Research Section A: Accelerators, Spectrometers, Detectors and Associated Equipment* 673 (2012), pp. 107–110. ISSN: 0168-9002. DOI: https://doi.org/10.1016/j.nima.2012.01.024. URL: https://www.sciencedirect.com/science/article/pii/S0168900212000642.

[26] H. Kolanoski and N. Wermes. *Particle Detectors: Fundamentals and Applications*. Oxford University Press, 2020. ISBN: 9780198858362.

[27] Fabian Königstein. “Bachelor thesis ”Simulation and analysis of cluster shapes in the ALPIDE monolithic active pixel sensor””. In: (2023).

[28] Jens Kröger, Simon Spannagel, and Morag Williams. *User Manual for the Corryvreckan Test Beam Data Reconstruction Framework, Version 1.0*. 2019. arXiv: 1912.00856 [physics.ins-det].

[29] S. Kushpil, F. Krizek, and A. Isakov. “Recent Results From Beam Tests of the ALPIDE Pixel Chip for the Upgrade of the ALICE Inner Tracker”. In: *IEEE Transactions on Nuclear Science* 66.11 (2019), pp. 2319–2323. DOI: 10.1109/TNS.2019.2945234.

[30] M. Mager. “ALPIDE, the Monolithic Active Pixel Sensor for the ALICE ITS upgrade”. In: *Nuclear Instruments and Methods in Physics Research Section A: Accelerators, Spectrometers, Detectors and Associated Equipment* 824 (2016). Frontier Detectors for Frontier Physics: Proceedings of the 13th Pisa Meeting on Advanced Detectors, pp. 434–438. ISSN: 0168-9002. DOI: https://doi.org/10.1016/j.nima.2015.09.057. URL: https://www.sciencedirect.com/science/article/pii/S0168900215011122.

[31] A. Maj. *Nuclear Physics Research At The Medical Proton Therapy Center CCB In Krakow.* Available at https://ispun23.vn/public/presents/Maj_ISPUN2023.pdf (2023/28/06). May 2023.

[32] R Mankel. “Pattern recognition and event reconstruction in particle physics experiments”. In: *Reports on Progress in Physics* 67.4 (Mar. 2004), p. 553. DOI: 10.1088/0034-4885/67/4/R03. URL: https://dx.doi.org/10.1088/0034-4885/67/4/R03.

[33] Silvia Masciocchi. *The Physics of Particle Detectors.* Lecture script of interaction of particles with matter. Heidelberg University, summer term 2022.

[34] Institute of Nuclear Physics PAN. *Cyclotron Centre Bronowice.* Available at https://ccb.ifj.edu.pl/en (2023/07/01).

[35] A. Prochazka. “Catima Physics Manual”. In: (2020).

[36] “Real-time data processing in the ALICE High Level Trigger at the LHC”. In: *Computer Physics Communications* 242 (2019), pp. 25–48. ISSN: 0010-4655. DOI: https://doi.org/10.1016/j.cpc.2019.04.011. URL: https://www.sciencedirect.com/science/article/pii/S0010465519301250.

[37] F. Reidt. “Upgrade of the ALICE ITS detector”. In: *Nuclear Instruments and Methods in Physics Research Section A: Accelerators, Spectrometers, Detectors and Associated Equipment* 1032 (2022), p. 166632. ISSN: 0168-9002. DOI: https://doi.org/10.1016/j.nima.2022.166632. URL: https://www.sciencedirect.com/science/article/pii/S0168900222002042.

[38] Kyrre Skjerdal and (forthe ALICE collaboration). “Photoproduction of ρ^0 in ultra–peripheral nuclear collisions at ALICE”. In: *Journal of Physics: Conference Series* 455.1 (Aug. 2013), p. 012010. DOI: 10.1088/1742-6596/455/1/012010. URL: https://dx.doi.org/10.1088/1742-6596/455/1/012010.

[39] A. Strandlie and W. Wittek. “Derivation of Jacobians for the propagation of covariance matrices of track parameters in homogeneous magnetic fields”. In: *Nuclear Instruments and Methods in Physics Research Section A: Accelerators, Spectrometers, Detectors and Associated Equipment* 566.2 (2006), pp. 687–698. ISSN: 0168-9002. DOI: https://doi.org/10.1016/j.nima.2006.07.032. URL: https://www.sciencedirect.com/science/article/pii/S0168900206013143.

[40] Herb Sutter. “A Fundamental Turn Toward Concurrency in Software”. In: *Dr. Dobb’s Journal* 30 (Mar. 2005), pp. 16–23. ISSN: 1044-789X.

[41] Tower Partners Semiconductor Co., Ltd. *Official website of Tower semiconductor*. Available at https://towersemi.com (2023/26/07).

[42] Martin Völkl. *Kalman Filtering*. Tutorial Slides of Kalman Filtering. Heidelberg University, winter term 2021.

[43] R. L. Workman et al. “Review of Particle Physics”. In: *PTEP* 2022 (2022), p. 083C01. DOI: 10.1093/ptep/ptac097.

[44] Weilin Yu. “Particle identification of the ALICE TPC via dE/dx”. In: *Nuclear Instruments and Methods in Physics Research Section A: Accelerators, Spectrometers, Detectors and Associated Equipment* 706 (2013). TRDs for the Third Millenium, pp. 55–58. ISSN: 0168-9002. DOI: https://doi.org/10.1016/j.nima.2012.05.022. URL: https://www.sciencedirect.com/science/article/pii/S0168900212005098.

[45] Gang Zhang et al. *The Measurement of Position Resolution of RD53A Pixel Modules*. 2019. arXiv: 1908.10973 [physics.ins-det].

Declaration

I declare that this thesis has been composed solely by myself. Except where states otherwise by references or acknowledgement, the work presented is entirely my own.

Erklärung

Ich versichere, dass ich diese Arbeit selbstständig verfasst und keine anderen als die angegebenen Quellen und Hilfsmittel benutzt habe.

Heidelberg, den 04.08.2023